The Dissertation Committee for Shuqiang Yang Certifies that this is the approved version of the following dissertation:

Field-driven and Spin-transfer-torque-driven Domain-Wall Dynamics in Permalloy Micro-/Nano- Structures

Committee:

James L. Erskine, Supervisor

Alejandro de Lozanne

John T. Markert

Llewellyn K. Rabenberg

Harry L. Swinney

Zhen Yao

Field-driven and Spin-transfer-torque-driven Domain-Wall Dynamics in Permalloy Micro-/Nano- Structures

by

Shuqiang Yang B.S.; M.S.

Dissertation

Presented to the Faculty of the Graduate School of
The University of Texas at Austin
in Partial Fulfillment
of the Requirements
for the Degree of

Doctor of Philosophy

The University of Texas at Austin
December 2007

Dedication

To my wife and my parents

Acknowledgements

I sincerely acknowledge the support of my Ph.D. supervisor, James L. Erskine for his continued guidance and encouragement. I would also like to thank Geoff Beach for the helpful discussions and Corneliu Nistor for his assistance on MOKE systems and domain-wall dynamic simulations. I would like to thank all the other member in our lab, David Lacina, Xubing Zhou, Aaron Cordes and Jusang Yang, for their assistance. Last but not least I would like to thank the members of my dissertation committee: Alejandro de Lozanne, John T. Markert, Llewellyn K. Rabenberg, Harry L. Swinney and Zhen Yao.

Field-driven and Spin-transfer-torque-driven Domain-Wall Dynamics in Permalloy Micro-/Nano- Structures

Publication No._____________

Shuqiang Yang, Ph.D.
The University of Texas at Austin, 2007

Supervisor: James L. Erskine

This dissertation explores magnetic-field- and electric-current-driven domain-wall motion in thin-film-based magnetic microstructures. Conventional thin-film growth and microstructure fabrication techniques including electron-beam lithography and focused ion beam milling are used to fabricate nanometer-scale one-dimensional and two-dimensional magnetic structures that support magnetic domains (regions of different magnetization orientation separated by domain walls). A high-spatial resolution, high-temporal resolution technique for measuring the field- or current- driven dynamics of the domain walls, based on the magneto-optic Kerr effect, is developed and used to study the wall dynamics.

Field-driven domain-wall motion at slow magnetic field sweep rates is dominated by Barkhausen jumps, the discontinuous random movement of domain-wall displacements. The experiments described represent one of the first successful attempts to extend the study of Barkhausen effects into the two-dimensional region. The experiments successfully probe velocity distributions, jump amplitude distributions, and attempt to address issues that pertain to the universal exponents that describe the scaling behavior of Barkhausen jump distribution function including effects of dimensionality and sweep-rate effects on the exponents.

A novel dual-beam magneto-optical experiment is performed on thin-film microstructure that probes negative Barkhausen jumps (jumps that oppose the direction favored by Zeeman energy driving the magnetic reversal). A new mechanism for negative Barkhausen jumps is proposed that accounts for the observed effects.

Domain-wall motion driven by (spin-polarized) electric current is studied in nano-scale thin-film based wires. The experiments address issues pertaining to the basic mechanisms responsible for current-driven domain-wall motion, which are believed to be the adiabatic spin-torque mechanism and non-adiabatic mechanisms. The experiments described are the first true time-resolved measurements of current-driven displacements, and the results reveal new information about the stochastic properties of current-driven domain wall displacements. The results also provide information on domain-wall velocities and spin-flip efficiencies that address issues related to spin-torque mechanisms.

Table of Contents

Chapter 1 Introduction 1

1.1 Basics of Ferromagnetism 2

1.2 Energies in a Ferromagnet 3

1.2.1 External Field (Zeeman) Energy 3

1.2.2 Exchange Energy 3

1.2.3 Anisotropy Energy 4

1.2.4 Magnetostatic Energy 5

1.2.5 Magneto-elastic Energy 6

1.3 Mircomagnetic Dynamics 6

1.4 Magnetic Domains and Domain-walls 8

1.4.1 Magnetic Domains 8

1.4.2 Magnetic Domain-walls 8

1.4.2 Bloch Wall and Néel Wall 10

1.5 Magneto-optical Kerr Effect 11

Chapter 2 Experimental Setup 14

2.1 Permalloy Film Deposition 14

2.1.1 Vacuum Chamber 14

2.1.2 Evaporators 16

2.2 Micro/Nano-structure Patterning 17

2.2.1 E-beam Lithography 18

2.2.2 FIB milling 18

2.3 MOKE Polarimeter 20

2.3.1 Optical Setup 20

2.3.2 Electronic Setup 25

2.3 MFM Setup 27

Chapter 3 Domain-wall Dynamics and Barkhausen Jumps in Thin-film Permalloy Microstructures 29

3.1 Introduction 29

3.2 Experiment 34
3.3 Results and Discussion 35
3.4 Summary..62

Chapter 4 Negative Barkhausen Jumps in Permalloy Thin-Film Microstructures 65
4.1 Introduction..65
4.2 Experiment...69
4.3 Results and Discussion 70
4.4 Conclusion 77

Chapter 5 Spin-Transfer-Torque-Driven DW Dynamics in Permalloy Nanowires 79
5.1 Introduction..79
5.2 Experiment...83
5.3 Results and Discussion 85
5.4 Additional Experiments 91
5.5 Conclusion 95

Bibliography 97

Vita 102

Chapter 1: Introduction

Magnetic domain-wall dynamics is a fundamental topic in magnetism and is closely related to an emerging nano-technology known as "spintronics"[1], e.g., novel magnetic devices where both spin and charge are involved in device functions. In addition to providing issues having fundamental scientific importance, magnetic domain-wall dynamics also provides important technological issues related to applications such as magnetic memory, magnetic recording media, magnetic reading/writing head, magnetic sensors, and so on.

Applying an external field is the conventional way to switch a magnet. Recently, manipulation of a domain-wall by electrical current (spin-transfer torque) is under intensive interest from the viewpoint of both fundamental physics and practical applications. This thesis describes both field-driven and spin-transfer-torque-driven domain-wall dynamics in thin film Permalloy micro-/nano-structures.

This thesis is organized as follows. The first chapter is an introduction of thin film magnetism. Chapter 2 describes the experiment setup, including device fabrication and the magneto-optical Kerr effect (MOKE) polarimeter. Chapter 3 describes experiments on field-driven domain-wall dynamics and Barkhausen Effect in Permalloy microstructures. Chapter 4 describes and explains an interesting phenomenon, negative Barkhausen jumps. The last chapter addresses the issues of spin-transfer-torque-driven domain-wall dynamics.

1.1 Basics of Ferromagnetism

The origin of Ferromagnetism remained a scientific mystery until the establishment of quantum mechanics. The classical mechanics interpretation of ferromagnetism is based on Weiss *molecular field* theory [2]. Weiss postulated there is a strong interaction field, which aligns the atomic moments in a common direction. Molecular field theory is able to explain the spontaneous magnetization and temperature-dependence phenomena, known as Curie-Weiss law. The Weiss molecular field is of the order of 10^9A/m, while a field as low as 10 ~ 100 A/m can switch a magnet. To resolve this discrepancy, Weiss proposed the idea of magnetic domains, a phenomenon that was confirmed by experiments later. For an individual domain, the magnetic moment direction is dominated by molecular field, while the orientations of domains can be different. The total moment is the average of all the domains and it can be any value between $\pm M_{spontaneous}$.

Weiss's theory gives us deep insight into ferromagnetism and in many cases it provides a sufficient approach to obtain desirable results. However, the origin of the molecular field cannot be explained by classical physics. The origin of molecular field can only be addressed by quantum mechanics, known as *exchange interaction* by Heisenberg [3]. The Pauli principle requires that the overall electron wave function to be anti-symmetric. If two electrons' spins are parallel (symmetric spin wave function), the real space wave function must be anti-symmetric. Namely, the two electrons can separate far away from each other to reduce Coulomb potential and this energy reduction is more significant. Therefore, in the end, origin of ferromagnetism is an electrostatic effect. Exchange interaction is described by Heisenberg Hamiltonian:

$$H = -\sum_{i,j} J_{ij} (\hat{S}_i \bullet \hat{S}_j) \qquad (1.1)$$

where J_{ij} is exchange constant and is positive for ferromagnets. $\hat{S}_i$ is electron spin momentum. Exchange interaction is short-range and usually we only consider this effect between neighbor spins. Equation (1.1) gives us the basic starting principle of ferromagnetism, however the situation in macroscopic magnet is more complicated and usually it is difficult to obtain desirable results from it directly. For the topics in this thesis, *micromagnetics* is an appropriate theoretical approach to address the issues.

Micromagnetics deals with magnetic systems as classical continuous objects with boundary conditions. Static and dynamic properties can be described by differential equations, which enables analytical and numerical simulation of magnetization dynamics. The energies in a magnet are essential for the micromagnetic equations; therefore the understanding of magnetic energy is the starting point for micromagnetics.

1.2 Energies in a Ferromagnet

There are several energy terms involved in a magnet and they can be either local or non-local. These energy terms interact each other and can produce complicated behaviors. The common energy terms are described below:

1.2.1 External Field (Zeeman) Energy

Zeeman energy is the interaction energy between magnetic moment and external field. The energy density is simply:

$$e_{Zeeman} = -\mu_0 \vec{H}_{ex} \cdot \vec{M} \tag{1.2}$$

where μ_0 is vacuum permeability, $\vec{M}$ is magnetization and $\vec{H}_{ex}$ is external field.

1.2.2 Exchange Energy

Exchange interaction (described in Equation (1.1)) favors magnetic moment alignment along a certain direction. Any deviation from this uniform alignment will cost energy. This energy is called exchange energy. Exchange energy density can be described as:

$$\begin{aligned} e_{exch} &= \frac{A}{M_s^2}(\nabla \vec{M})^2 \\ &= \frac{A}{M_s^2}(|\nabla M_x|^2 + |\nabla M_y|^2 + |\nabla M_z|^2) \end{aligned} \tag{1.3}$$

where M_s is the magnitude of saturated magnetization, A is a material constant, known as exchange stiffness constant. For isotropic Heisenberg exchange interaction A is a scalar, otherwise A is a tensor. Usually isotropic exchange interaction is accurate enough to describe practical systems.

1.2.3 Anisotropy Energy

The energy of a magnet depends on the magnetization direction. The symmetry breaking behavior is called anisotropy. For bulk materials, the intrinsic anisotropy (magnetocrystalline anisotropy) is mainly due to spin-orbit coupling. This interaction depends on the spin direction relative to the lattice and also the symmetry of the crystal. There are several magnetic anisotropy energies listed below:

(i) Uniaxial Anisotropy

Uniaxial anisotropy is very common in thin film samples. The anisotropy strength can be controlled in many cases, so it is very useful to improve the properties of a device. For bulk materials, hexagonal and tetragonal crystals exhibit uniaxial anisotropy. The uniaxial anisotropy energy density term can be written as:

$$e_{Ku} = K_{u1}\sin^2\theta + K_{u2}\sin^4\theta \tag{1.4}$$

where θ is the angle between the anisotropy axis and the magnetization direction. K_{u1} and K_{u2} are material constant in unit of J/m^3. Higher order terms can be added, while K_{u2} and higher order terms are commonly neglected.

(ii) Cubic Anisotropy

For a cubic crystal, the anisotropy energy density is:

$$e_{Kc} = \frac{K_1}{M_s^4}(M_x^2 M_y^2 + M_y^2 M_z^2 + M_z^2 M_x^2) \qquad (1.5)$$

If $K_1 > 0$, <100> is easy axis, otherwise <111> is easy axis.

(iii) Exchange Anisotropy

Exchange anisotropy usually occur when ferromagnetic and anti-ferromagnetic materials co-exist. The exchange coupling between these two phases produces unidirectional anisotropy. Unlike the other anisotropy above, exchange anisotropy is asymmetrical. The coupling results in a shifted hysteresis loops shifted by a factor, known as exchange field. The exchange anisotropy energy is in the form of:

$$e_{ex} = -K_{ex} \cos\theta \qquad (1.6)$$

where K_{ex} is a constant and θ is the angle between magnetization direction and the anisotropy preferred direction.

(iv) Surface Anisotropy

The symmetry breaking of the surface atoms can induce an anisotropy energy term, known as surface anisotropy, which is described by:

$$e_s = K_s(1 - |\vec{M} \cdot \hat{n}|^2) \qquad (1.7)$$

where K_s is in unit of J/m^2 and $\hat{n}$ is the surface normal direction. Surface anisotropy can be neglected in bulk samples and thick films.

1.2.4 Magnetostatic Energy

Magnetostatic energy (also known as: stray field energy, demagnetization energy, or magnetic dipolar energy) arises from the field generated by the magnet. We can calculate "magnetic charge" by the divergence of magnetization, so magnetostatic energy is similar to electrostatic energy. Magnetostatic energy is a non-local term; therefore it causes some difficulties for analytical and numerical solutions. Particularly for numerical simulations, this term costs more computing time. Magnetostatic energy can be calculated by:

$$E_{dm} = \frac{1}{2}\mu_0 \int_{\infty} H_{dm}^2 dV = -\frac{1}{2} \int_{sample} \vec{H}_{dm} \cdot \vec{M} dV \tag{1.8}$$

where H_{dm} is magnetostatic field (stray field). More explicitly, magnetostatic field energy density can be expressed as:

$$e_{dm} = \frac{1}{8\pi}\mu_0 \vec{M}(\vec{r}) \cdot [\int_{volume} \nabla \cdot \vec{M}(\vec{r}') \frac{\vec{r}-\vec{r}'}{|\vec{r}-\vec{r}'|^3} d^3 r' - \int_{surface} \vec{M}(\vec{r}') \cdot \hat{n} \frac{\vec{r}-\vec{r}'}{|\vec{r}-\vec{r}'|^3} dS'] \tag{1.9}$$

1.2.5 Magneto-elastic Energy

Changing magnetization can induce a deformation of a magnet and the stress in a sample can induce anisotropy energy. For Permalloy ($Ni_{80}Fe_{20}$), this effect is weak; therefore magneto-elastic energy can be neglected.

1.3 Mircomagnetic Dynamics

Micromagnetic dynamics deals with the spin dynamic reaction under a torque. For an angular momentum, the reaction will be a processional (gyroscopic) motion. This motion can be simply described by:

$$\frac{\partial \vec{M}}{\partial t} = -\gamma \vec{M} \times \vec{H}_{eff} \tag{1.10}$$

where $\gamma = \frac{g\mu_0 e}{2m_e}$ is gyromagnetic ratio and $\vec{H}_{eff}$ is the effective field. The Lande factor g is usually close to 2. This equation describes a ceaseless processional motion and it is obviously not the case in reality. In reality, the spin will eventually relax to an equilibrium orientation in the direction of the effective field. Therefore there must be some energy loss (damping). In order to account for energy loss, a damping term must be added in equation (1.10). There are two forms of the damping term: Gilbert damping and

Landau-Lifshitz damping. With Gilbert damping, the micromagnetic dynamic equation is:

$$\frac{\partial \vec{M}}{\partial t} = -\gamma_G \vec{M} \times \vec{H}_{eff} - \alpha_G \frac{1}{|\vec{M}|} \vec{M} \times \frac{\partial \vec{M}}{\partial t} \tag{1.11a}$$

and with Landau-Lifshitz damping, the equation is:

$$\frac{\partial \vec{M}}{\partial t} = -\gamma_{LL} \vec{M} \times \vec{H}_{eff} - \alpha_{LL} \gamma_{LL} \frac{1}{|\vec{M}|} \vec{M} \times (\vec{M} \times \vec{H}_{eff}) \tag{1.11b}$$

These two equations are called Landau-Lifshitz-Gilbert (LLG) equation and they are proved [4] to be equivalent. Figure 1.1 shows the spin dynamic behaviors described by equation (1.10) and (1.11).

Figure 1.1 Spin precession under a field (a): spin precession without damping described by equation (1.10).(b): spin precession with damping described by equation (1.11).

It should be noted that $\vec{H}_{eff}$ is the total internal magnetic field that includes anisotropy fields and other contributions. It is different from the applied field and it is not trivial to calculate it. For micromagnetic dynamic numerical simulations, calculation of $\vec{H}_{eff}$ is one of the key issues. Specifically $\vec{H}_{eff}$ is given by:

$$\vec{H}_{eff} = -\frac{1}{\mu_0} \frac{\partial e_{total}}{\partial \vec{M}} \tag{1.12}$$

where $e_{total} = e_{Zeeman} + e_{anisotropy} + e_{exch} + e_{dm}$ (magneto-elastic energy is neglected).

1.4 Magnetic Domains and Domain-walls

1.4.1 Magnetic Domains

The idea of a magnetic domain was first provided by Weiss [2] and domain theory was first developed by Landau and Lifshitz [5]. The origin of domains is to reduce magnetostatic energy. Figure 1.2 illustrates a single domain and a closure domain sample. The single domain sample produces more stray field and has higher magnetostatic energy. Stray field energy is eliminated (at the expense of anisotropy energy and exchange energy in domain walls) by forming closure domains.

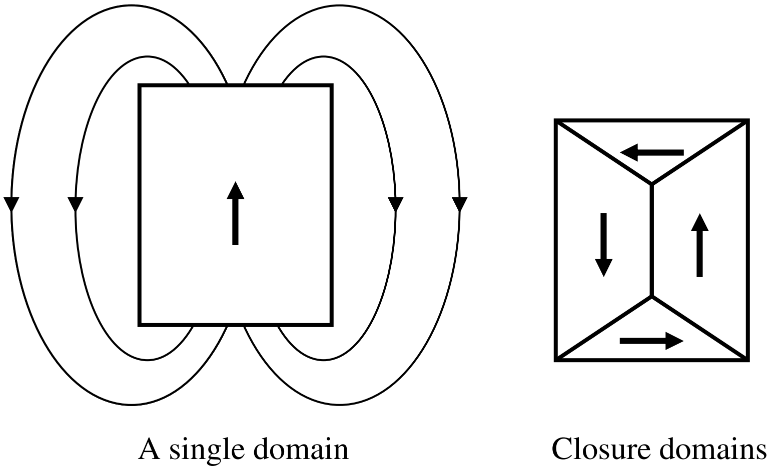

Figure 1.2 A single domain sample has higher magnetostatic energy than a closure domain sample

Usually domain formation will increase E_{exch} and $E_{anistropy}$. The equilibrium domain structure is the competition between the various energy terms above.

1.4.2 Magnetic Domain-walls

A magnetic domain-wall is the narrow region where the spins rotate from the direction of one domain to the other. The exchange energy tends to favor a thick wall, while the anisotropy energy tends to favor a thin wall. The domain-wall thickness is the competition between exchange energy and anisotropy energy. Next we will justify this conclusion as in [6]. Let us consider a 180^0 domain-wall in a uni-axial anisotropy sample. Assume the domain-wall thickness (δ) contains n layers of spin. Namely $\delta = na$, where a is the lattice constant. We also assume the angle between neighbor spins in the wall is a constant $\theta = \frac{\pi}{n}$ and the anisotropy energy density in the wall is a constant K. This is a simplified assumption, because in reality both θ and K are not constants, but it can give us a good estimation. θ should be a small angle, so from equation (1.1) the exchange energy of a pair of spin is:

$$-2JS^2\cos\theta = JS^2\theta^2 - const \tag{1.13}$$

The constant above can be ignored. There are $\frac{n}{a^2}$ spins in a wall in unit area. So the exchange energy in unit area of a wall is:

$$E_{exch} = \frac{n}{a^2} JS^2\theta^2 = \frac{\pi^2 A}{na} \tag{1.14}$$

where $A = \frac{JS^2}{a}$ is exchange stiffness constant.

The anisotropy energy of a wall is given by:

$$E_{anis} = K \cdot (\text{ the volume of a wall in unit area}) \quad = K\frac{1}{a^2}na^3 = Kna \tag{1.15}$$

The total energy is:

$$E_{wall} = E_{exch} + E_{anis} = \frac{\pi^2 A}{na} + Kna \tag{1.16}$$

and n is the variable. The wall energy is a minimum with respect to n.

$$\frac{\partial E_{wall}}{\partial n} = -\frac{\pi^2 A}{n^2 a} + Ka = 0 \longrightarrow n = \frac{\pi}{a}\sqrt{\frac{A}{K}} \tag{1.17}$$

The wall thickness $\delta = na = \pi\sqrt{\frac{A}{K}}$ (1.18)

The typical wall thickness is a few hundred nanometers. The wall energy is:

$$E_{wall} = 2\pi\sqrt{KA} \tag{1.19}$$

1.4.3 Bloch Wall and Néel Wall

There are mainly two types of domain-wall structure: Bloch Walls and Néel Walls, although there are some variations from these two walls, such as crosstie walls. In a Bloch wall, the spins rotate in the wall plane, while in a Néel wall the spins rotate through the wall plane. Figure 1.3 shows the two types of walls. From the figure, we can see the demagnetization energy of a Bloch wall in a thick film or bulk sample is lower. While in a thin film, the demagnetization energy will align the wall spins in the plane of film, e.g. a wall.

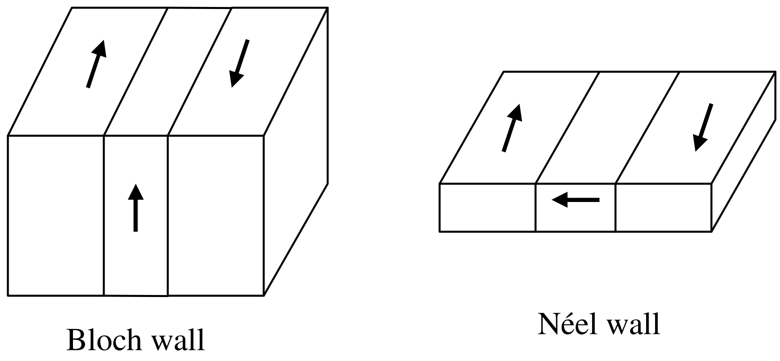

Figure 1.3 Block Walls and Néel Walls. In thick samples, a Block wall has lower demagnetization energy. In thin samples, a Néel wall has lower demagnetization energy

1.5 Magneto-optical Kerr Effect

Magneto-Optical Kerr Effect (MOKE) polarimetry is one of the main tools used to probe spin dynamics in our experiments. To better understand the data in this thesis, the MOKE technique is described in this chapter.

When a polarized light beam is reflected from a smooth magnetic surface, depending on the surface magnetization of the sample and the beam orientation, the polarization direction and intensity of the reflected beam will change by a small amount. This effect is known as the MOKE.

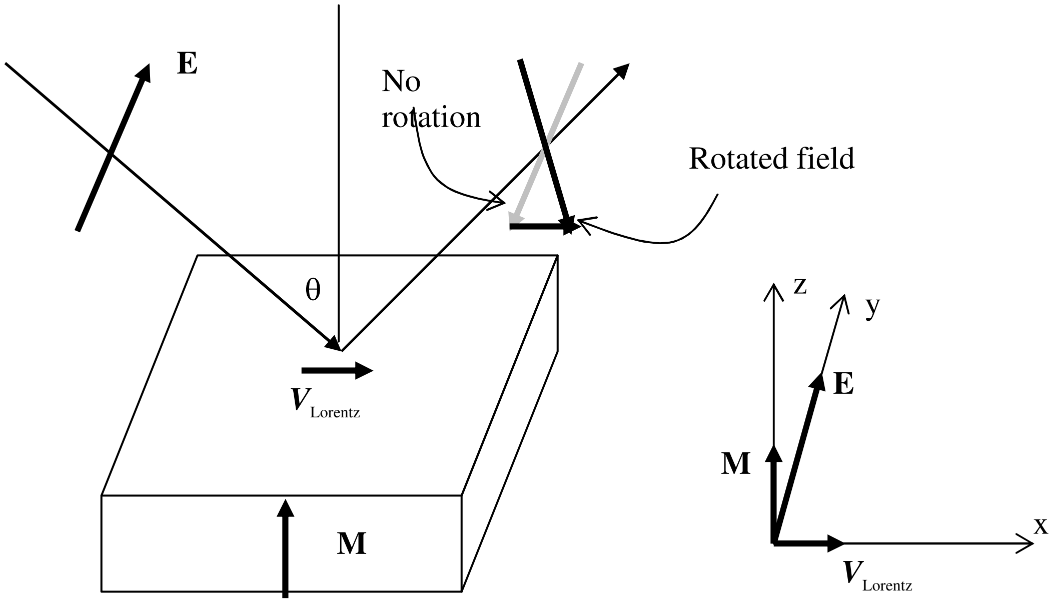

Figure 1.4 Lorentz motion acting on the electrons will make the polarization of the reflected light rotate. ***E*** *is the electrical field in the light.* ***M*** *is the magnetization of the sample.*

The MOKE can be described by a simple analysis based on the Lorentz force applied on the light-driven electrons [7] (the actual mechanism depends on spin polarization (not the applied H-field) and spin-orbit coupling). Figure 1.4 gives an example, where the incident light is in *s* polarization and the magnetization is in *polar* orientation (perpendicular to the surface). The electron primary motion is in the electrical field (**E**), while a transverse motion is induced by the Lorentz force due to the magnetic moment of the sample. The velocity of this Lorentz motion is proportional to the magnetization. Specifically, $\boldsymbol{v}_{\text{Lorentz}}$ is proportional to $\mathbf{E} \times \mathbf{M}$. In Figure 1.4, the Lorentz motion will make the polarization of the reflected light rotate counterclockwise (facing the light).

There are three high-symmetry orientations of the magnetization: polar, longitudinal and transverse. They are shown in Figure 1.5. In addition, the incident light can be *s* or *p* polarized. Therefore there are six basic configurations for MOKE experiments. By the analysis similar to Figure 1.4, we can obtain all the results for the six configurations, which are shown in Table 1.1.

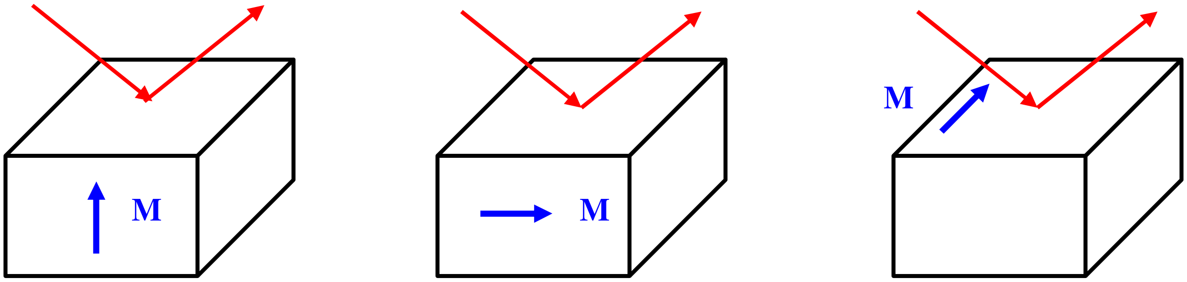

(a) Polar (b) Longitudinal (c) Transverse

Figure 1.5 Three orientations of the sample magnetization

M orientation Light polarization	Polar	Longitudinal	Transverse
s	Rotates c.c.w. Maximum rotation when $\theta = 0$	**Rotates c.w.** **Rotation $\propto \sin\theta$**	No effect
p	Rotates c.c.w. Maximum rotation when $\theta = 0$	Rotates c.c.w. Rotation $\propto \sin\theta$	No rotation Intensity will change

Table 1.1 MOKE results for the six basic configurations. (c.c.w means counter-clockwise and c.w. means clockwise rotation facing the light). For the experiments in this thesis, the MOKE is s-polarized and longitudinal mode (bold font text in the table).

For quantitive MOKE calculation, we can start with the permittivity tensor [7]. For cubic materials the tensor is given by:

$$\varepsilon_{Kerr} = \varepsilon \begin{bmatrix} 1 & -iQm_3 & iQm_2 \\ iQm_3 & 1 & -iQm_1 \\ -iQm_2 & iQm_1 & 1 \end{bmatrix}$$

Where ε is the vacuum permittivity, Q is the Voigt constant and m_i is the components of the unit magnetization vector in the coordinate of cubic lattice. Q is very small for common materials, in the order of 0.01, and proportional to saturation magnetization. Based on this tensor, Maxwell equations and boundary conditions, we can calculate the rotation and phase shifts of the reflected light.

Chapter 2: Experimental Setup

This chapter describes the general features of our experiments. For a specific experiment, there might be some additional variations. The main experimental tools include: film deposition, micro-/nano-structure patterning, MOKE polarimeter and Magnetic Force Microscopy (MFM).

2.1 Permalloy Film Deposition

2.1.1 Vacuum Chamber

Permalloy films are deposited in an Ultra-High Vacuum (UHV) chamber. Two roughing pumps, a turbo molecule pump, an ion pump and a Titanium sublimate pump are installed on this chamber. After baking the chamber, the best pressure can reach the range of 10^{-11} Torr. Usually the films are deposited at a pressure of 10^{-9} Torr. Figure 2.1a shows a schematic top view of the chamber. Besides the Permalloy evaporation source, a Gold/Chromium source and a Tantalum source can be installed for capping layers and producing electrical contact-lead films. Auger electron spectroscopy is available to analyze the surface chemical composition and Low Energy Electron Diffraction (LEED) can be used to characterize epitaxial samples. The samples are oriented in the vertical direction and can be rotated around the vertical axis to face the growth sources and analytical/characterization tools. Figure 2.1b shows a picture of the chamber and the controller panels.

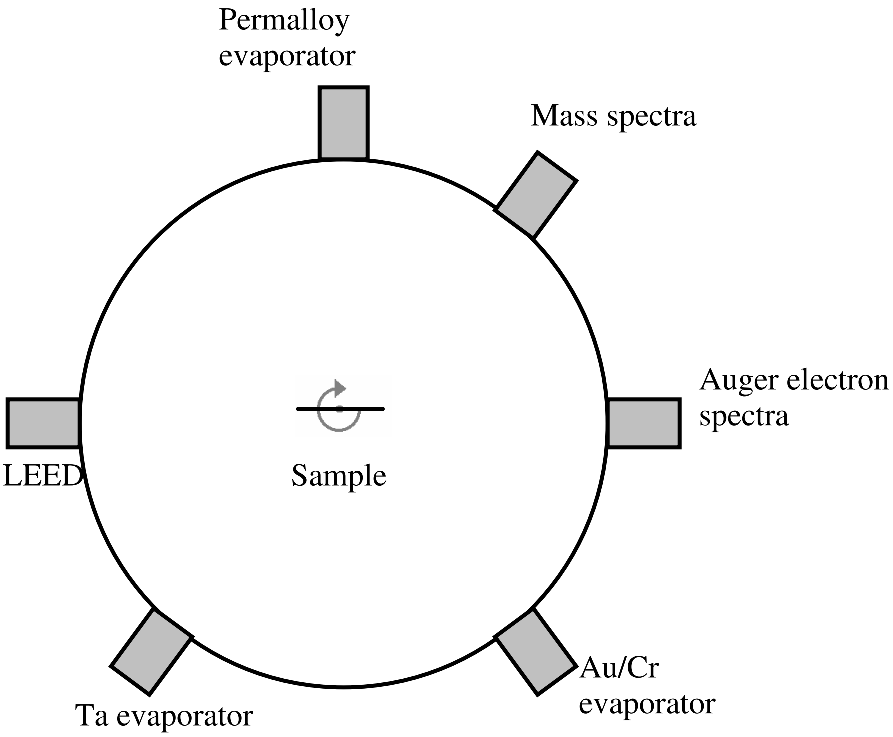

(a) schematic top view

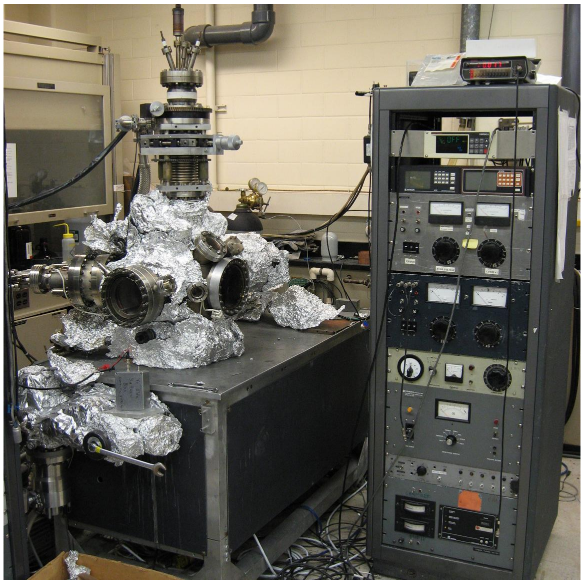

(b) A picture of the chamber and the controller panels

Figure 2.1: Film deposition chamber

2.1.2 Evaporators

(i) E-beam evaporator

Permalloy or Ta films are deposited by e-beam heating evaporation. Figure 2.2 shows the principle of an e-bean evaporator. The filament (resistance ~ 1 Ohm) is heated by a high-current AC power supply resulting in thermionic emission. The source is positively biased by a high voltage supply, and the emitted electrons (e-beam) are accelerated toward the source. The electrons' kinetic energy is transformed into thermal energy at the source. The heating power is proportional to the bias voltage and the e-beam current.

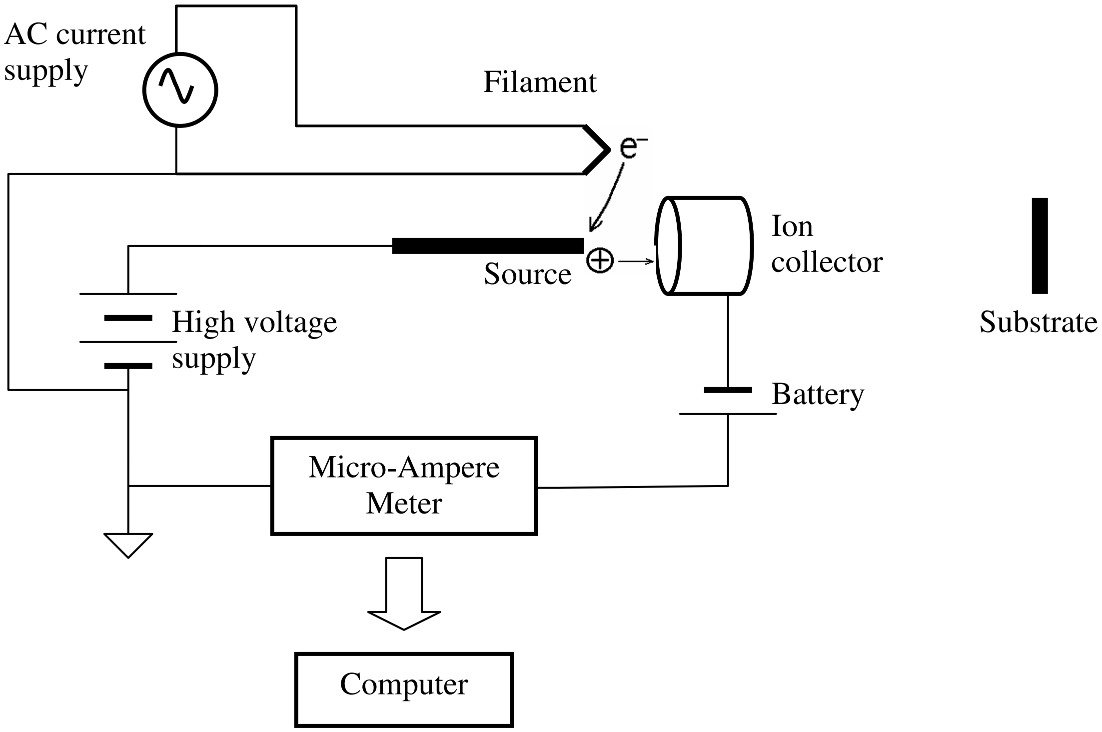

Figure 2.2: Schematic drawing of an e-beam evaporator

When the source temperature is high enough, atoms are evaporated from the source; some atoms are ionized by the e-beam, and these ions can be used as a flux monitor. We can obtain the relationships below:

$$\left.\begin{array}{l} I_{ion} \propto I_{atom} \times I_{e\text{-beam}} \\ \text{Film-thickness} \propto \int I_{atom}\,dt \end{array}\right\} \quad \text{Film-thickness} \propto \int I_{ion}\,dt$$

where I_{ion} is the flux of ions, I_{atom} is the flux of atoms and $I_{e\text{-beam}}$ is the e-beam current. Therefore the film thickness can be monitored by collecting the source ions. As shown in Figure 2.2, a collector is biased at –60V by a battery. The ion current is measured by a micro-Ampere meter. A computer reads the current and integrates it. After calibration, the film thickness can be monitored with 5% error. Compared to the common crystal thickness monitor, the advantages of this method include: there is no temperature drift; we do not need to change crystals at certain time intervals; the structure is more compact and no water-cooling system needed.

(ii) Thermal evaporator

Au and Cr are deposited by thermal evaporation from a resistively-heated tungsten filament. The thickness is monitored by a crystal monitor. This method is the conventional evaporation technique, but it requires that the source material must not form an alloy with the W filament and this limits its application.

2.2 Micro/Nano-structure Patterning

Micro/Nano-structures can be patterned by either E-beam Lithography or Focused Ion Beam (FIB) milling. The choice of which method depends on the specific requirements of the microstructure being prepared.

2.2.1 E-beam Lithography

Figure 2.3a describes the procedure for E-beam Lithograph patterning. First, e-beam resist PMMA (polymethyl methacrylate) is coated on the substrate by spin coating. The coating thickness depends on the spin-speed and the concentration of PMMA solution. Usually 200~300 nm thickness coating is used in our experiments. Then the substrate is exposed by a commercial Raith50 E-bean Lithography system. The e-beam energy is 20 KeV and the smallest structure (e-beam focus size) that can be fabricated is about 100nm. After exposure, the substrate is developed by 1:3 (MIBK: alcohol) solution. The exposed part is dissolved into the solution. And then the substrate is placed in our vacuum chamber and the film is deposited on the whole sample. After the film deposition, the sample is placed in boiling acetone to remove the unexposed part. Eventually only the structure defined by the electron beam exposure is left.

The process above is simple, but when the film is deposited, the edge of the deposited structure will contact the PMMA and this contact can induce roughness at the final structure edge. Figure 2.3b shows a dual coating-layer processing for resolving this problem. The under coating layer (copolymer) is more sensitive to the e-beam. Therefore the developed area is broader. During the film deposition, no contact is involved.

2.2.2 FIB milling

During FIB milling, a scanning Ga ion beam is focused on a sample. The energy of the Ga ions is high enough to knock out the target atoms. Figure 2.4 shows the procedures for FIB milling patterning.

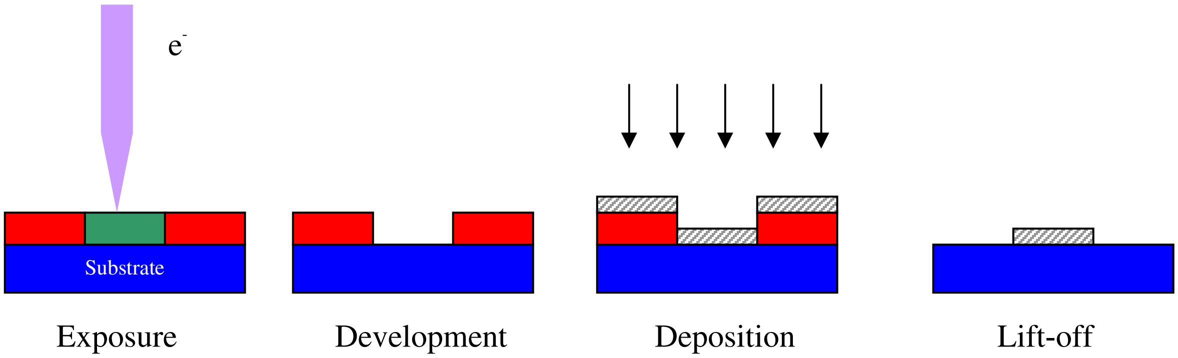

(a) Single coating-layer e-beam lithograph procedures

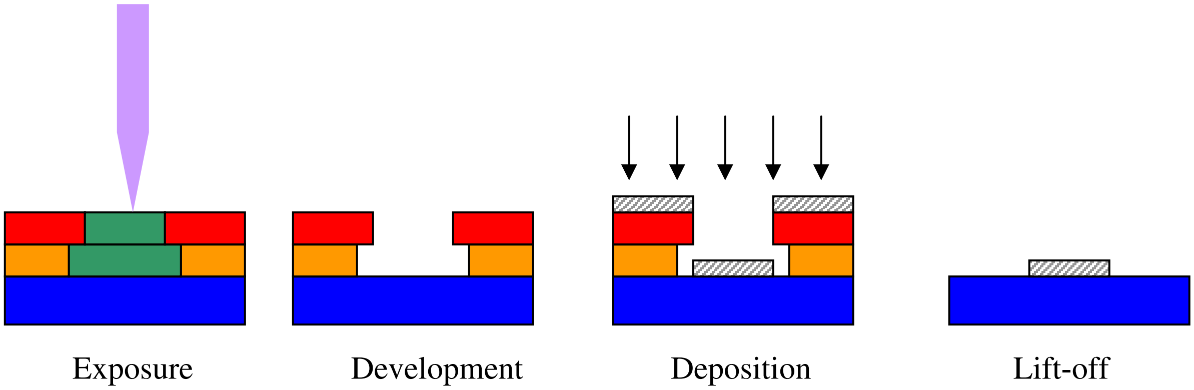

(b) Dual coating-layer e-beam lithograph procedures

Figure 2.3: Procedures for E-beam Lithograph patterning

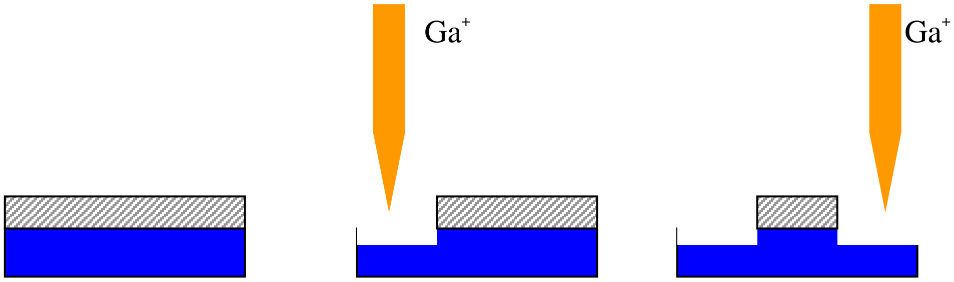

Figure 2.4: Procedures for FIB milling patterning

2.3 MOKE Polarimeter

MOKE polarimeter is used to measure the time-dependent magnetic properties of our samples. It has advantages of high temporal resolution, high sensitivity (can detect the magnetization in a volume of 10^{-19} m^3) and high spatial resolution. There is a trade-off between temporal resolution (bandwidth) and S/N ratio. The polarimeter discribed in this thesis is used to study the stochastic properties (no signal-averaging is allowed). In this application the highest temporal resolution is about 300ns with S/N ratio ~ 20. For low frequency measurement, the S/N ratio can reach 100. Figure 2.5 shows a schematic diagram and a picture of the MOKE polarimeter.

2.3.1 Optical Setup

The light source of the early experiment is a He-Ne laser. Recently it has been replaced by a single longitudinal mode solid state laser. Compared with the He-Ne laser, the statistical noise is significantly smaller. The wavelength is 658 nm and the output power is about 50mW. We choose this red light laser, because the photo detector (discribed below) is more sensitive to long wave-length light.

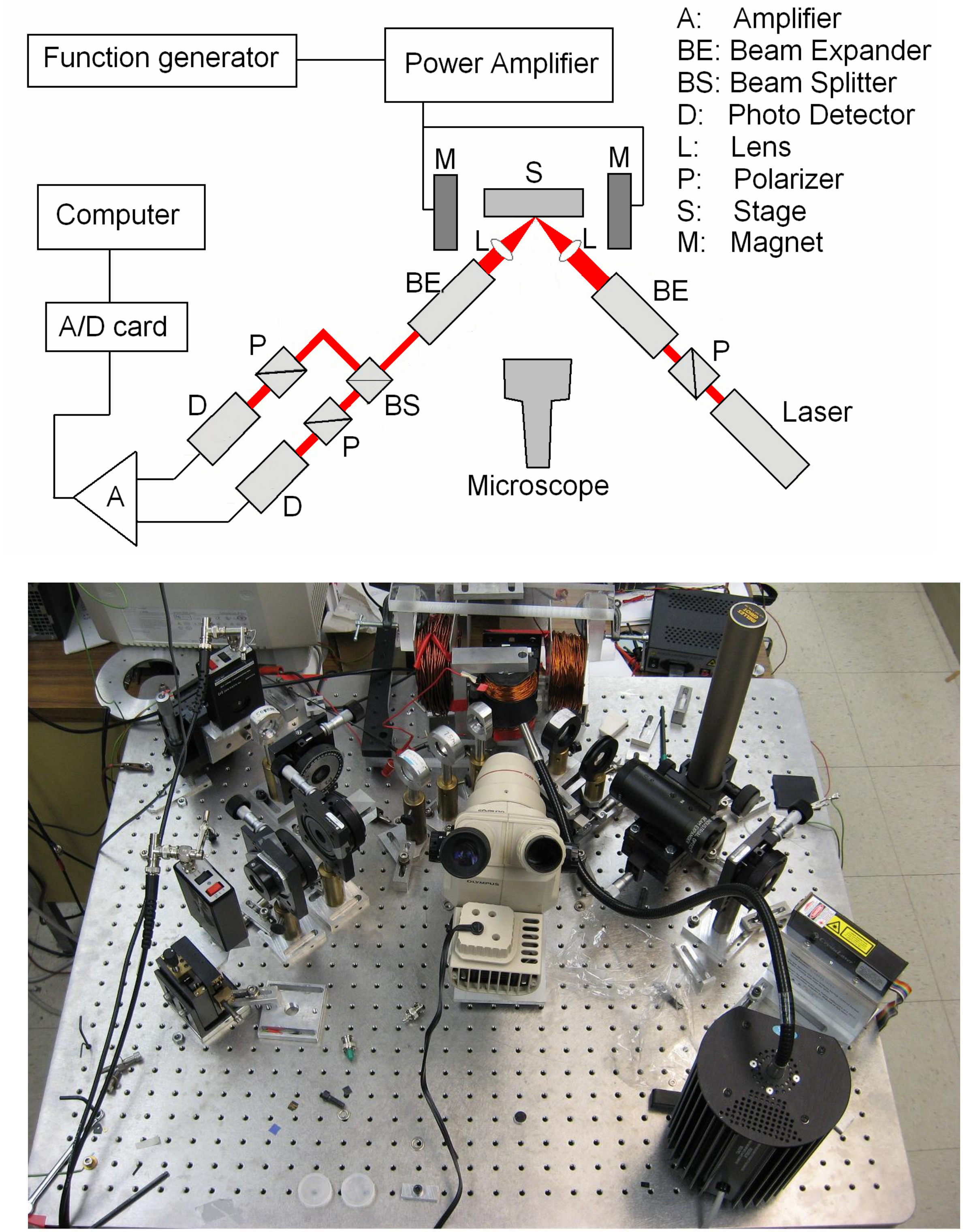

Figure 2.5: A schematic diagram and a picture of the MOKE polarimeter

The laser beam is polarized by a Glan-Taylor prizm polarizer (extinction ratio ~ 10^{-5}). The polarization is in the direction vertical to the table (s polarization). After the polarizer, a commercial ×20 beam expander is used to increase the beam diameter, because larger numerical aperture is needed to obtain a small focus spot on samples. The objective lens is a 25 mm diameter double-let achromatic lens with a 75mm focus-length. The beam incident angle is 45^0, therefore the spot on a sample is an ellipse. The minimum length of the ellipse major axis is about 10μm. If a smaller spot is needed, the lens can be replaced by a high quality microscope objective lens. Samples are mounted on a comercial two-dimension translation stage with a precision of 1 μm. This stage is used to move the sample into the view of the laser beam. The reflected beam from the sample is collected by a plane-convex lens and the beam becomes parallel again. The beam diameter is too large for the following optical devices, therefore a beam expander (inverse orientation) is used to shrink the beam size. A ×3 homemade beam expander is used, which contains a plane-convex lens (75mm focal length) and a plane-concave lens (25mm focal length) as shown in Figure 2.6.

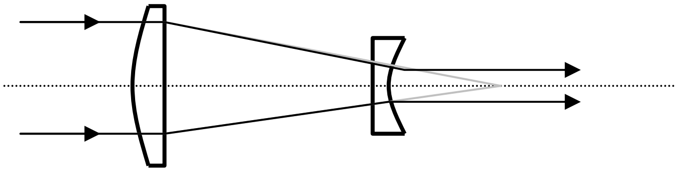

Figure2.6 A ×3 beam expander (inverse orientation)

A 50/50 non-polarizing beam splitter is inserted after the beam expander to divide the main beam into two equal sub-beams, which are sent to two Glan-Taylor polarizers (P+ and P-). The polarization angles (angle from null direction) of P+ and P- are α and $-\alpha$ respectively. The advantage of this arrangement is: the common signals, (such as the fluntuation of the laser and microphonic/vibrational effects) are eliminated; while the two Kerr signals are differential and their amplitudes add.

The kerr signal and noise can be analyzed in a simple way as below:

Lignt intensity on a detector: $I = A^2 \sin^2\alpha + I_0$, where α is the angle of the polarizer (analyzer) measured from extinction and I_0 is the transmitted light intensity at extinction due to finite extinction ratio and we can treat it as a constant.

Kerr signal (light intensity change): $dI = 2A^2 \sin\alpha \cos\alpha \, d\alpha$, where the small angle $d\alpha$ is Kerr rotation.

Assuming optical noise (such as shot noise) is proportional to the square root of light intensity, we have noise from photons:

$N_{optical} = c\,(I)^{1/2} = c\,A \sin\alpha$, where c is a constant.

Therefore, overall $S/N = (2A^2 \sin\alpha \cos\alpha \, d\alpha)/(N_{optical} + I_0 + N_{electronic}) = (2A^2 \sin\alpha \cos\alpha \, d\alpha)/(c\,A \sin\alpha + I_0 + N_{electronic})$, where $N_{electronic}$ is the noise due to electronic devices (such as Johnson noise and 1/f noise).

If $N_{electronic}$ can be neglected, the optimum α to maxmize S/N ratio depends on I_0. Typical values of α in this case are a few degrees. However, in actual experiments, we find $N_{electronic}$ can be considerable large and cannot be neglected. Generally speaking, to improve S/N, a larger α is needed for a larger $N_{electronic}$, while α should not be larger than 45^0 and photo detector can also be possible to be saturated at large α.

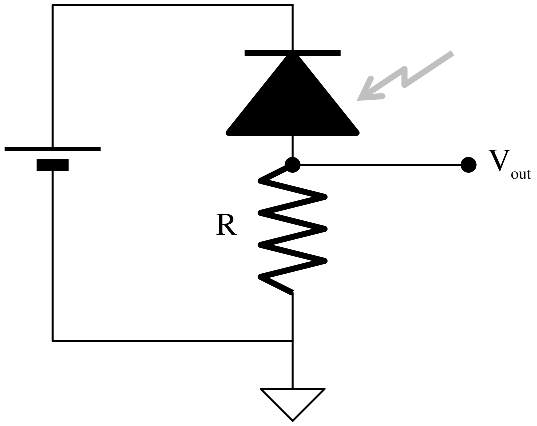

Figure 2.7 Schematic of a Si photo detector

The photo detectors are a pair of Silicon photo diodes. As shown in Figure 2.7, the resistor R determines the sensitivity and bandwidth of the detector. A large R can improve S/N, while it reduces the bandwidth. In our experiment, 1 kOhm R is chosen to match the bandwidth of the differential pre-amplifier (>1MHz).

At last, a microscope is installed to help focusing the beam and locating the micro/nano-structures. A fiber lamp is used for the illumination of the microscope.

If low temperature measurement is needed, samples must be placed in a vacuum chamber. This MOKE system can be transferred to the vacuum chamber, with the objective lens and collection lens replaced by long focal length lenses. The sample must be mounted on a translation stage to enable precise position adjustment. Because the common commercial stage cannot be placed in the UHV system (due to outgas and baking issues, etc), we made a vacuum sample holder as shown in Figure 2.8.

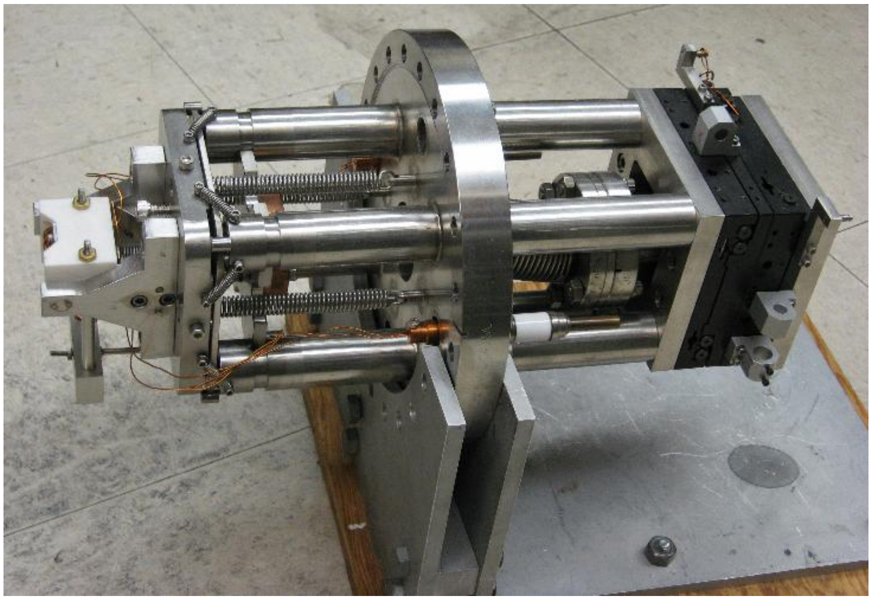

Figure 2.8 A sample holder for measurement in vacuum

This sample holder contains a homemade stainless-steel UHV translation stage on the inner side of the flange and a commercial translation stage on the outer side of the flange. The motion of the outer stage can be translated to the inner stage by a lever between them. Samples are mounted on a piece of Macor with a magnet built in. The Macor assembly can rotate around a horizontal axis for optical alignment and is mounted on the inner stage.

2.3.2 Electronic Setup

The electronic setup mainly includes a data acquisition system, a magnet system and a fast pulse generator.

- *Data acquisition*

Because the Kerr signal is very weak, a Stanford Research Systems SRS560 low noise differential preamplifier is connected to the photo detectors. Depending on the signal amplitude and noise level, the gain is usually set to a value between 500 and 5000. The output of the amplifier is sent to a 14-bit and 100MHz bandwidth Gage-14100 A/D card. The 14-bit resolution provides high enough precision to detect typical Kerr signals. If higher speed is needed, a 1GHz bandwidth Lecroy digital oscilloscope can be used to replace the Gage card. The computer program is written in C++ language. Besides data acquisition, this program can do real time signal processing. For example, in some experiments, intensity fluctuations are evaluated in real time and if the noise is abnormally large, the data is discarded.

- *Magnet system*

Two magnets are used in the MOKE system to produce in-plane orthogonal magnetic fields. The magnets are Helmholtz coils driven by a Kepco power amplifier. A waveform generator is used to drive the Kepco amplifier. The generator is Stanford

Research Systems DS345 with a bandwidth of 30 MHz. Usually only the horizontal magnet is used to magnetize the samples, while in some cases (see Chapter 5), both magnets are needed to generate field pulses in sequence. For this two-magnet system, we can definitely use another generator-amplifier system to drive the second magnet. However, to save the investment on these instruments, two parallel diodes are inserted at the power amplifier to select an individual magnet, as shown in Figure 2.9.

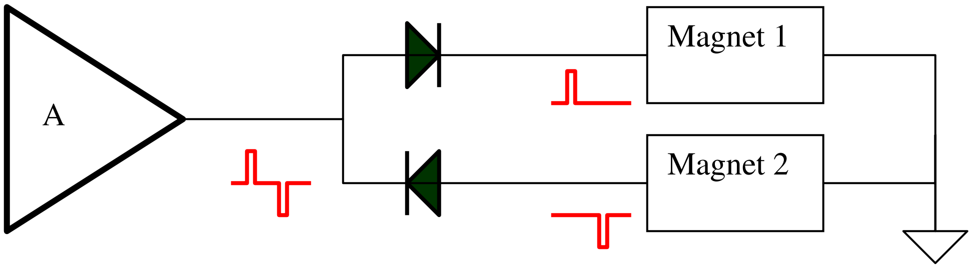

Figure 2.9 Two diodes are use to select an individual magnet

- *Fast pulse generator*

Fast pulse generator is needed for spin-transfer-torque-driven domain-wall dynamics (see Chapter 5). The pulse is used to apply a current through Permalloy nano-wires. We can use the waveform generator to generate a short pulse. However, the pulse amplitude (uni-polar 20V, bi-polar 10V) is too small and the speed (35ns rise time) is too low in some cases. We built a high amplitude (uni-polar 40V) and high-speed (10ns rise time) pulse generator based on an analog relay. The analog relay is a microchip manufactured by Maxim Company. A waveform generator is used to drive it, as shown in Figure 2.10.

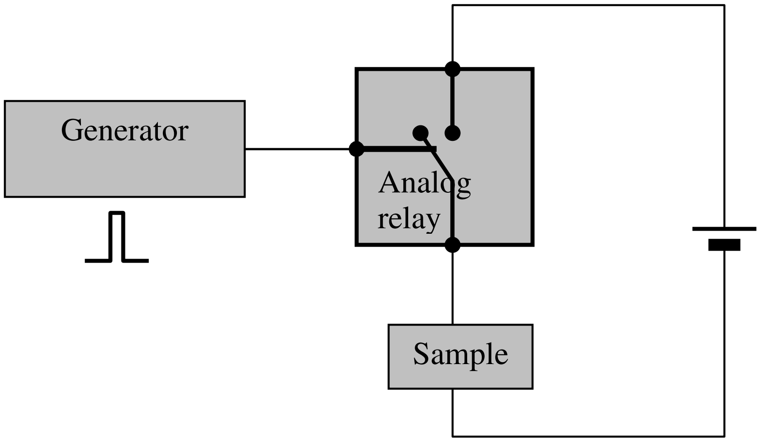

Figure 2.10 A pulse generator built by a analog relay

2.4 MFM (Magnetic Force Microscope) Setup

A commercial MFM (Veeco® MultiMode SPM) is used to observe domain structures in our samples. A MFM can image the domain-walls by scanning a tip (coated with a ferromagnetic film) at the proximity of the sample surface. The tip is like a magnetic dipole, which can interact with the stray field from a domain-wall. The magnetic moment of the tip is an important parameter to be considered. A high moment tip can give strong signal, while the field from the tip might be so large that the domain-walls are dragged away. Permalloy is a very soft ferromagnetic material and we observed that a medium moment (1×10^{-13}emu) tip could drag away the domain-walls; therefore we selected the low moment (0.3×10^{-13}emu) tip for our experiments.

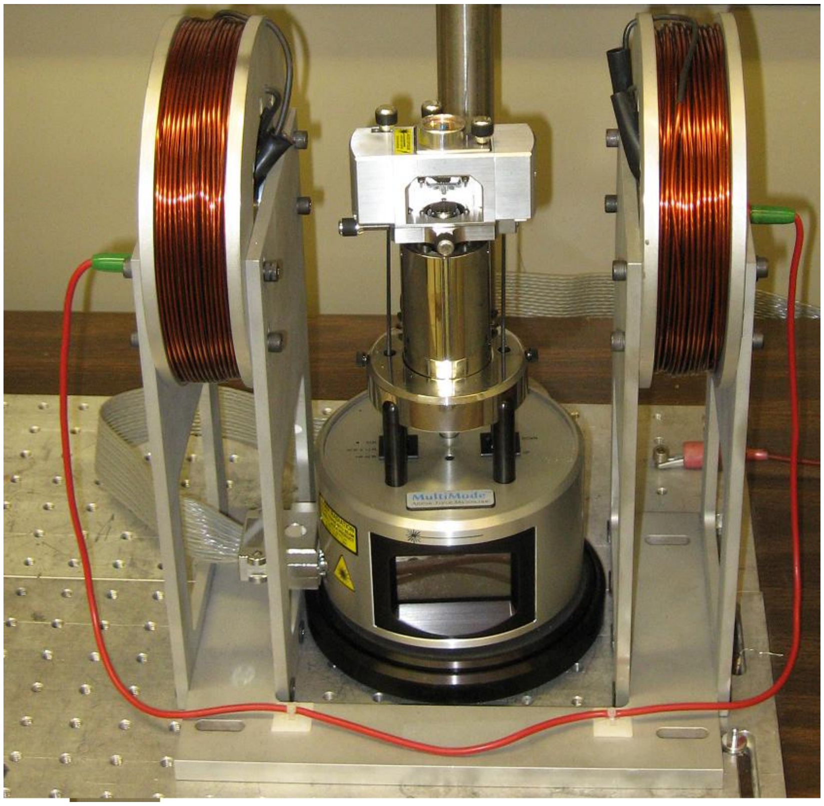

Figure 2.11 A MFM with a magnet on it

To observe domain structures at different field, a homemade magnet (Helmholtz coils) is added on the MFM system, as shown in Figure 2.11. The maximum field generated from the magnet is about 50 Oe. The magnet is driven by a Kepco power amplifier controlled by a computer with a D/A card.

Chapter 3: Domain-wall Dynamics and Barkhausen Jumps in Thin-film Permalloy Microstructures

3.1 Introduction

The random changes in magnetization resulting from irreversible stochastic motion of domain-walls (DWs) during field-driven magnetization reversal are known as the Barkhausen Effect (BE), named from scientist who made the first observation [8]. Before the development of domain observation technology, the discovery of BE was an indirect evidence of Weiss's domain hypothesis. Figure 3.1 schematically shows Barkhausen Jumps in a hysteresis loop.

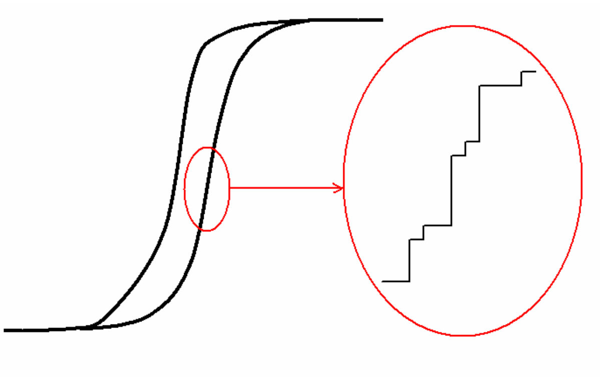

Figure 3.1: The reversal of a magnet consists of random abrupt changes in magnetization, known as the Barkhausen Effect.

A detailed description of the BE, and closely-related ferromagnetic hysteresis, at the level of nanometer-scale interactions of domain-walls with lattice defects, impurities and surface/interface features that can act as domain-wall pinning centers continues to present difficult challenges. However, phenomenological descriptions of the BE [9-12] and magnetic hysteresis [13-15] now provide remarkably simple expressions for domain-wall velocities, BE jump-amplitude distribution functions and various scaling laws that can be experimentally tested. Specifically, power-law functions describing probability distributions, including drive-frequency-dependent scaling behavior associated with the BE have been measured in bulk samples and in many cases have been shown to be in good agreement with theoretical predictions [9-11]; related experiments have explored correlation effects in BE avalanches and concepts of self-organized criticality [16]. Nearly all of these results have been obtained using bulk samples in which eddy-current damping governs domain-wall mobility and in which the probed sample volume is large $(1\ \mathrm{mm})^3$ and determined by the induction pick-up coil technique used in the experiments.

The BE experiments reported in this chapter (published at Physical Review B [85]) are carried out in a different regime using thin-film microstructures in which eddy-current damping is negligible, and where the probed sample volume is precisely defined and much smaller than a typical bulk-sample grain size. The absence of eddy-current damping in thin films and thin-film based structures permits very high domain-wall velocities during Barkhausen jumps (BJs) that are limited (as demonstrated in this chapter) by local spin-damping mechanisms. This feature plays a role in determining sweep-rate dependent exponents that characterize BJ statistical distributions and may help account for the striking differences apparent from a simple visual comparison (page 17, Ref. 9) of BN spectra of bulk and thin-film samples: BJ spectra for thin films exhibit very sharp peaks of short duration with no detectable structure whereas bulk materials produce BJ spectra with jagged structure characteristic of avalanche behavior.

The results presented in this chapter are discussed within the framework of two models: a domain dynamics model developed by Alessandro, Beatrice, Bertotti and

Montorsi (ABBM) [10], and a generalization of the ABBM model (that includes dimensionality) described by Cizeau, Zapperi, Durin, and Stanley (CZDS) [11]. The ABBM model considers a rigid domain-wall in stochastic pinning potentials. The CZDS model deals with elastic domain-walls and consider the magnetic dipole interactions in a sample. The ABBM model provides a good basis for describing the velocity distributions, based on a mobility equation, and the power law sweep-rate dependencies that describe jump amplitude distributions. However, the low sweep-rate (adiabatic) value of the velocity distribution exponent obtained from our experimental results suggest that the thin films and thin-film microstructures studied in work reported in this chapter behave as two-dimensional (2-d) systems which are more appropriately described by the CZDS model. A starting point for summarizing the underlying assumptions and features of the ABBM model and understanding the experimental data presented in this chapter is the classic result obtained by Williams, Shockley and Kittel [17] in which it was shown that the average field-driven domain-wall motion at slow sweep rates is governed by a mobility relationship:

$$<\upsilon_{dw}> = \xi(H - H_0) \tag{3.1}$$

where H is the external applied field, and H_0 is a threshold field that includes internal counter fields of various origins including demagnetizing fields, domain-wall interactions with pinning centers and DW-DW interactions. The parameter ξ is the DW mobility. In thick metallic ferromagnetic films, DW damping is governed by eddy-currents [17] with energy dissipation that scales as $M_s^2\ \upsilon^2\ \Delta x^2/\rho$ and mobility that scales as $\rho/(M_s\Delta x)$ where M_s = saturation magnetization, Δx = thickness, and ρ = resistivity. In very thin films, (Δx < few hundred Å), the mobility increases until limited by a different (local) damping mechanism which we show to be the intrinsic spin-damping mechanism that is incorporated in the LLG equations in the form of a dimensionless parameter, α_G.

The ABBM [10] model generalizes Eq. (3.1) by postulating that the instantaneous DW velocity is governed by a similar equation:

$$\upsilon_{dw} = \xi'(H - (H_{dm} + H_p)) \qquad (3.2)$$

where the geometry-dependent demagnetizing field, H_{dm}, is separated from a random component, H_p that includes all short-range counterfield contributions. The mobility parameter ξ' in Eq. (3.2) should be viewed as a statistical parameter with a maximum value ξ'_{max} governed by a suitable spin-damping mechanism. The pinning field, H_p, is assumed to exhibit statistical properties governed by details of the local pinning potentials that inhibit DW motion. The DW motion resulting from a uniformly-increasing applied field (dH/dt = constant) can be obtained analytically from this model yielding, among other predictions, scaling functions [11,12] that govern the distribution of DW velocities (υ), Barkhausen Jump (BJ) amplitudes (ΔM), and durations ($\Delta\tau$):

$$P(\upsilon) = \upsilon^{-\alpha} f(\upsilon/\upsilon_0) \qquad \alpha = 1 - c \qquad (3.3)$$

$$P(\Delta M) = (\Delta M)^{-\beta} f(\Delta M/\Delta M_0) \qquad \beta = 3/2 - c/2 \qquad (3.4)$$

$$P(\Delta\tau) = (\Delta\tau)^{-\gamma} f(\Delta\tau/\Delta\tau_0) \qquad \gamma = 2 - c \qquad (3.5)$$

where $c \propto dH/dt$ is a dimensionless parameter that characterizes the sweep rate, and $f(X)$ is a cutoff function. The parameters υ_0, ΔM_0 and $\Delta\tau_0$ can be related to various materials-dependent properties such as correlation lengths, conductivity, spin-damping parameters and differential permeability.

In the ABBM model of DW motion, the parameter c determines the general characteristics of the probability distributions. In the adiabatic limit ($c \rightarrow 0$) the probability distributions for DW velocity, BJ amplitude and duration become universal power law functions. In the ABBM model, these exponents (from Eqs. (3.3-3.5)) are $\alpha = 1$, $\beta = 3/2$ and $\gamma = 2$. In this limit, DW motion is characterized by intermittent jumps described by the distribution functions, Eqs. (3.3-3.5). In the limit c>>1, statistical effects are suppressed and the DW is assumed to move at a constant average velocity $<\upsilon>$ described by Eq. (3.1). The condition c = 1 defines crossover from the regime (c<<1) of intermittent jumps to (c>>1) continuous motion. It is reasonable to assume that under suitable constraints or assumptions, that Eq. (3.1) and Eq. (3.2) would both provide an accurate description of DW processes. Our experiments indicate that the mobility equation, Eq. (3.1), can accurately describe averaged statistical distributions based on Eq. (3.2) by introducing an exponent q that allows nonlinear scaling of the applied field dependence, or by assuming that the mobility ξ depends on sweep rate.

Experiments on bulk magnetic samples carried out using flux pick-up coils are capable of detecting BE signals with sufficient sensitivity and dynamic range (over three decades in the jump-amplitude ΔM, for example) to accurately test the scaling function predictions of the ABBM model, Eqs. (3.3-3.5) [9-12, 14, 16]. The pick-up coil technique measures flux changes that accompany BJs, and several assumptions and approximations are required to quantitatively interpret the measured BN jump-amplitudes (pick-up coil voltage $\propto d\phi/dt$) in terms of absolute BJ volumes and velocities associated with DW motion [18]. This chapter discribes measurements of DW phenomena in permalloy thin-film microstructures that achieve sufficient temporal resolution and sensitivity to directly measure DW velocities of individual BJs and BN jump-amplitude distributions. These measurements permit a sensitive and direct experimental test of Eq. (3.2), as well as additional tests of the scaling laws Eqs. (3.3-3.5) and theories of universal scaling exponents on a spatial scale corresponding to 0.1% of the volume of a typical bulk-sample grain size. The films studied are thin enough (thickness = 220 Å) to suppress eddy-current damping, and our experiments, therefore, probe all of these effects in a spin-damping regime that is different from eddy-current damping in bulk samples. We are able to demonstrate that the maximum value of the mobility parameter (ξ' in Eq. (3.2)) is governed in the thin-film limit by the local (gyromagnetic) damping mechanism. Our experimental results also demonstrate the limits of Eq. (3.1) (linear, nonstochastic model) for accurately describing DW dynamics, and explore selected features of the distribution function exponents associated with Barkhausen effects in thin-film geometry

3.2 Experiment

Domain-wall motion and hysteresis loops were measured using a high-speed high-spatial resolution magneto-optic Kerr effect (MOKE) polarimeter incorporated into a long-focal-length polarized-light microscope [19]. The polarimeter components were recently up-graded to optimize the sensitivity for BE measurements: relevant components include a 20 mW He-Ne laser, small area (nanosecond response) silicon photodetectors and wide-band low-noise preamplifiers. Under typical operating conditions (Figs. 3.2C, 3.2D), measurement of BE jump-amplitudes, defined by $\Delta M/M$, with a signal-to-noise (S/N) ratio of slightly above 10:1 was achieved using an effective sampling time of 0.2 μsec. Under these conditions, the noise floor was amplifier Johnson-noise limited, but near the shot-noise limit. The polarimeter response was calibrated by measuring the 10% - 90% risetime of a square wave produced by modulating the laser intensity using a pockels cell (20 nsec risetime, checked with a 1 nsec photodiode and fast oscilloscope). The linear-ramp (sawtooth) magnetic field was produced by Helmholtz coils driven by a bipolar power supply. The Kerr effect signal was digitized by a fast oscilloscope (8 bit/1GHz band width) and transferred to a PC for processing.

Digital averaging of data (binning of adjacent A/D samples) was used, in some cases, to improve the sensitivity (signal/noise ratio (S/N)) at the expense of temporal resolution in order to detect small BJs (compare noise floor of Fig. 3.2A and Fig. 3.2B for example).

The magnetic sample used in our experiments was a $200 \times 200\ (\mu\mathrm{m})^2 \times 220$ Å thick microstructure of permalloy grown by UHV electron-beam vapor deposition on a high-quality commercially-polished Si(100) ±0.5° wafer. Standard e-beam lithography plus lift-off techniques were used to create several microstructures of slightly different sizes and shapes. Some experiments were also carried out on similarly prepared continuous 300Å thick films. Similar sample preparation and measurement techniques were recently used to study hysteresis loss scaling of permalloy microstructures over a wide drive-field frequency range (10^{-2} – 10^{6} Hz) [15]. The sample used in the BE experiments reported in this chapter exhibited the same typical low static coercivity (~ 0.5 Oe) and simple domain patterns common to permalloy thin-film microstructures [15, 20,21].

3.3 Results and Discussion

Figure 3.2 displays representative measured changes in magnetization produced by BJs during field-driven magnetization reversal of the microstructured sample. The laser beam was focused to illuminate the entire sample area within the diameter that corresponds to half of the total flux. Therefore, all BJs created by the sample during magnetization reversal having amplitude above the noise floor were detected. Later it is demonstrated that the temporal resolution achieved in our experiments was sufficiently high to determine the maximum theoretical velocity of a DW during a BJ.

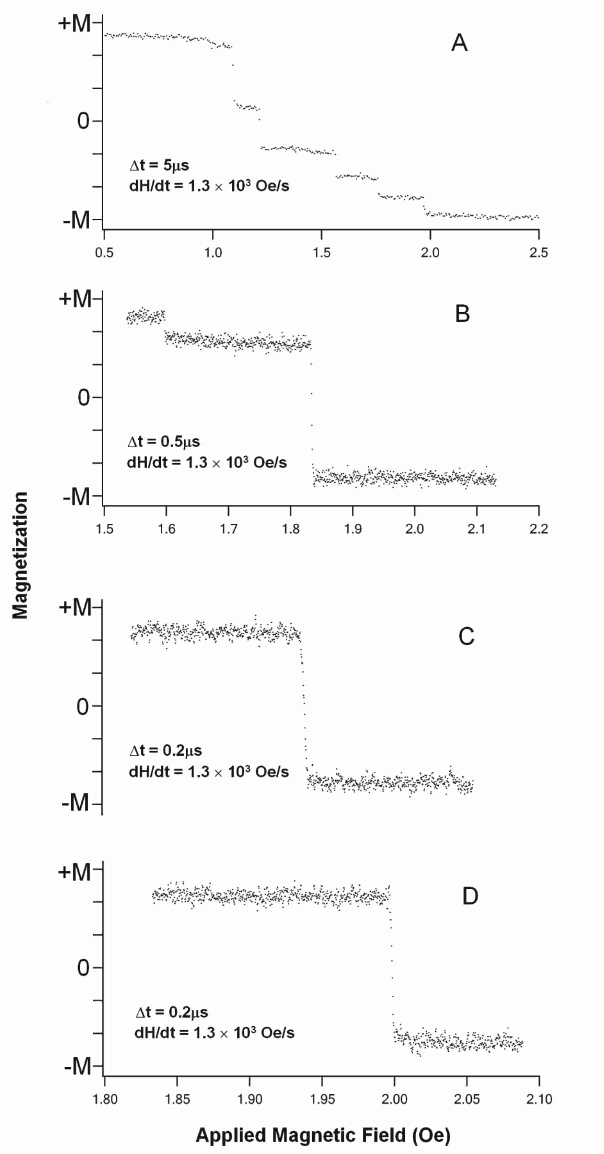

Figure 3.2: Typical magnetic reversal transients M(t) that exhibit Barkhausen jumps. The temporal resolution, Δt parameter (each panel) corresponds to the integration time interval between M(t) samples (each point). Note scale changes in horizontal axis (Applied Field). The magnetization axis corresponds to $<M_x>$,

the total average sample magnetization parallel to the applied field. The lower two panels C and D display single large fast (C) and faster (D) transients (υ for panel D is ~ 150 m/sec). The Johnson noise for (A) corresponds to N~2% (2M); for (B) N~10% (2M).

The well-defined spatial scale of the microstructured thin-film samples and the MOKE method employed to detect BJs offers the opportunity to carry out DW velocity measurements based on a model that relates DW velocity to measured values of ΔM: $v_{DW} = (\Delta \mathrm{M}/2\mathrm{M})^{\pi} L/\tau$ where L is a spatial scale parameter, and τ and ΔM/2M are the switching transient time and fractional change in magnetization resulting from a BJ. The parameter π permits analysis in terms of a one-dimensional model ($\pi = 1$) in which a DW is assumed to sweep across the viewed area, or a two-dimensional model ($\pi = 1/2$) in which a DW encloses an area where M abruptly changes. In the limit of large jumps ($\Delta\mathrm{M}/2\mathrm{M} \to 1$) both models yield the same calculated velocity.

In our experiments, the spatial scale L is determined by the sample size ($L = 200\mu$m) and ΔM/2M and τ are obtained directly from the BE jump-amplitude (Fig. 3.2). We explored both model limits ($\pi = 1$ and $\pi = 1/2$) and observed no qualitative differences in the velocity distributions. Since the laser beam diameter was adjusted to cover the entire microstructure, $\pi = 1/2$ was judged more appropriate for the smaller BJs, and used to obtain the velocities described later and plotted in Fig. 3.5. We note that the distribution functions $\mathrm{P}(\Delta\mathrm{M})$ (displayed in Fig. 3.3) and the scaling exponents obtained from them and discussed later are not affected by the choice of π. Obviously, an experimental velocity distribution function (i.e., Eq. (3.3)) would reflect model dependencies, but the velocity exponents are not obtained or discussed in the present

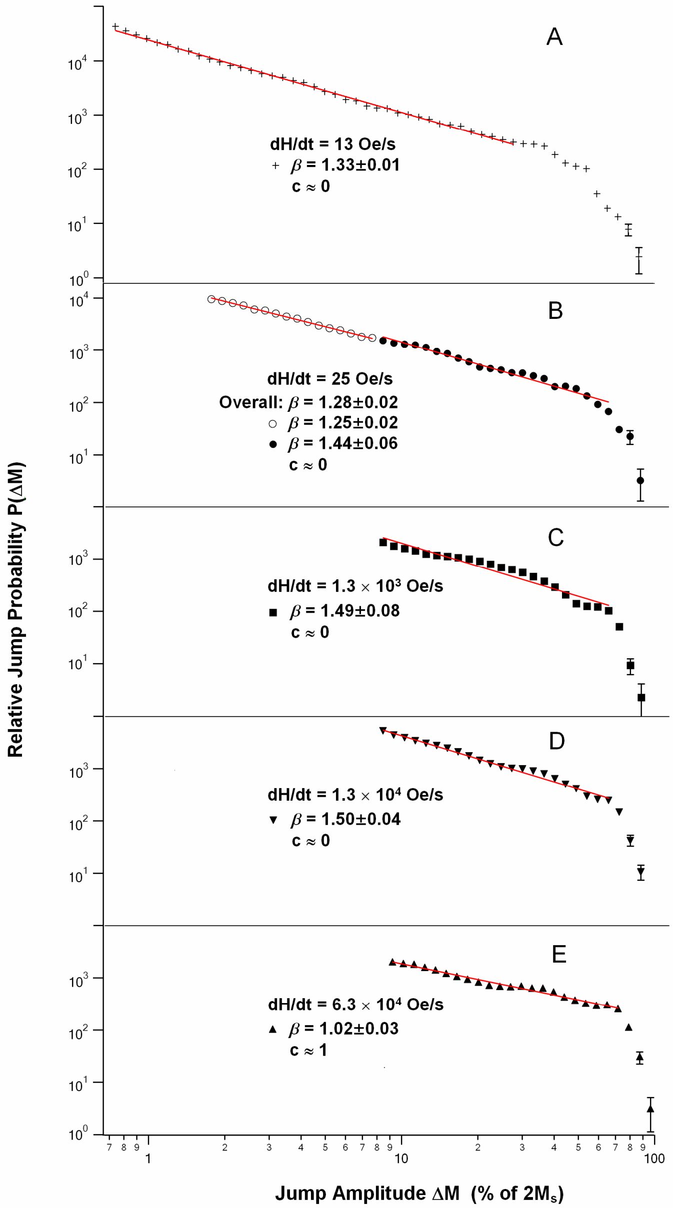

Figure 3.3: Log-log plots of relative jump probability P(ΔM) vs jump amplitude ΔM. Values of scaling exponent β obtained from fitting data (using Eq. (3.4) without cutoff function) and value of sweep parameter c deduced from the values of β (refer to text) are displayed for each sweep rate. Open circles in Panel B

correspond to extension of data set by binning procedure described in text. Symbol size represents error bars except where indicated. The data set displayed in Panel A was obtained using a 50 mW solid state laser and is described in Subsection c. Note that that uncertainty assigned to the value of β is the precision of the fit based on chi-square values and not the accuracy of the determined value of β.

chapter. The maximum DW velocity (discussed later) occurs for measured values of ΔM/2M~1 where model dependencies do not matter. Also, in cases where the choice of π or the experimental noise floor, which limits detection small BJs, could affect a conclusion (i.e., discussion related to Fig. 3.6), these dependencies were explored.

Figure 3.3 displays log-log plots of BE jump-amplitude probability P(ΔM) vs jump-amplitude ΔM for linear-ramp sweep rates ranging from 13 Oe/sec to 63 kOe/sec (1 Hz – 5 kHz saw tooth waveform). Each set of jump-amplitude probabilities P(ΔM) vs. ΔM for a given value of sweep rate, dH/dt, was obtained from a computer-based search of about 10^4 half-cycle measurements of field-driven magnetization reversal. The smallest BE jump-amplitudes recorded correspond to the threshold criteria ΔM≥ factor of 2 above the noise floor. This criterion applied to the S/N level of typical ΔM transients measured at low sweep rates (for example, Fig. 3.2A) results in ΔM resolution of better than 5% and a dynamic range of 20. The binning procedure, described in the experiment section, was used to extend the S/N ratio for the13 Oe/sec and 25 Oe/sec drive-field frequency data (refer to M(t) data displayed in Fig. 3.2A), which accounts for the extended range of P(ΔM) vs ΔM plots in Fig. 3.3A and 3.3B. Each bin in the P(ΔM) histograms is based on well over 100 BJ events except for the last 3 or 4 bins (where ΔM is large and near 2M). Therefore, the statistical errors in P(ΔM) values are below 10% except where indicated by error bars.

Curve fitting of the distributions using Eq. (3.4) (based on a strict power law without a cut-off function) yields the values of β and c displayed with each P(ΔM) distribution. The straight-line fits to at least 20 values of P(ΔM) for ΔM<0.7(2M) corresponding to the determined values of β are indicated on the graphs, with error estimates that reflect the precision of the power-law fit based on chi-square analysis. The BE jump-amplitude probability distributions (Fig. 3.3) depart from power-law behavior over a very narrow range of jump amplitudes (cutoff regions are represented by only 3 or 4 data points) and the relative jump probability of these few points is low resulting in significantly larger statistical errors indicated by error bars.

We conclude this section with a discussion of data presented in Fig. 3.3B-3.3E leading to the estimate c~1 at $\frac{dH}{dt} \sim 6.3\text{x}10^4$ Oe/sec and $\beta = 1.45 \pm 0.05$ at c=0 based on a power-law fit neglecting the cutoff behavior. Results for the extended-range P(ΔM) data (Fig. 3.3A, 3.3B) are discussed later. Due to the limited dynamic range of our experimental data at the sweep rates above 25 Oe/sec, the P(ΔM) power-law scaling only covers about 1 decade for the higher sweep rates. While the precision of the power-law fit is good (refer to chi-square values, Table 3.1), the accuracy of the value obtained from the fit can be strongly affected by the range of data available and by the cutoff function. We return to these issues after a brief discussion of relevant theoretical and experimental work on critical exponents presented in the subsection that follows.

Power Law Fit (excluding last three points)

dH/dt	β	Chi square
25 Oe/sec	1.44 ± 0.06	0.092
25 Oe/sec*	1.28 ± 0.02	0.14
1.3 x 10^3 Oe/sec	1.49 ± 0.08	0.20
1.3 x 10^4 Oe/sec	1.50 ± 0.04	0.047
6.3 x 10^4 Oe/sec	1.02 ± 0.03	0.032

Power Law Fit (with cutoff, M_o=83, $\eta = 10$)

DH/dt	Chi square	
	$\beta = 1.5$	$\beta = 1.28$
25 Oe/sec	1.3	0.98
1.3 x 10^3 Oe/sec	1.3	1.8
1.3 x 10^4 Oe/sec	0.74	0.55
6.3 x 10^4 Oe/sec	0.88	0.38
	$\beta = 1.0$	
6.3 x 10^4 Oe/sec$^+$	0.12	

Table 3.1: Power law fits to data shown in Figs. 3.3 and 3.4. All fits cover ~ 1 decade, 20 values of $P(\Delta M)$ *except where noted (by *). Chi-square values for top panel (power law fit, no cutoff) show good precision for determination of* β*. Lower panel shows chi-square results for fits to two models:* $\beta = 1.5$ *and* $\beta = 1.28$ *without dH/dt scaling including the cutoff parameters indicated. Last entry (+) shows that chi-square fit improves significantly when* $\beta = 1$ *is used for the highest sweep-rate distribution.*

The minor departures of $P(\Delta M)$ from power-law behavior (away from the cutoff region) are common features associated with microstructures. Lateral size constraints begin to limit the allowed domain configurations and this effect can add structure to log-log plots of $P(\Delta M)$ vs ΔM representing disruption of the power-law behavior of $P(\Delta M)$. In very small microstructures, the single-domain limit is reached in which $P(\Delta M)=1$ and $\Delta M=2M$. The size of the microstructure used in our experiments was selected to reduce these effects allowing extraction of distribution function scaling exponents and comparison with those obtained from studies of bulk samples and continuous film systems.

The values of c and β displayed in Fig. 3.3 are estimated using the same one-decade range of ΔM values for each sweep rate by first noting that β is essentially constant (and described by $\beta = 1.45 \pm 0.05$) for drive field frequencies f = 2, 100, 1000 Hz (Fig. 3.3B - D), suggesting c << β, and then using $\beta = 1.50 - c/2$ with $\beta = 1.0 \pm .05$ obtained from the 5000 Hz $P(\Delta M)$ fit (Fig. 3.3E), (yielding c ~ 1 at 5 kHz). Based on this analysis, our experiment detects frequency-dependent scaling of β over the sweep rate range from 25 to $6.3\text{x}10^4$ Oe/sec, where β=1.5 corresponding to c << 1 for the lower sweep-rates, and β=1.0 corresponding to c=1 at the highest sweep rate. This interpretation is consistent with the ABBM model exponent behavior, Eq. (3.4).

a. Critical Exponents

The sweep-rate dependence of β and the $c \rightarrow 0$ limit estimate of $(\beta \sim 1.5)$ obtained for our permalloy thin-film microstructure, demonstrated by the results presented in Fig. 3.3, merit further discussion. Despite the large number of publications describing BN phenomena, the number of reliable estimates of critical exponents is limited [9]. In addition, dimensional crossover [22,23], current understanding of sweep-rate dependencies [11,24], cutoff phenomena, and generally the role of dimensionality in BN phenomena remain controversial. The recent review of Durin and Zapperi [9] presents a comprehensive picture of the current status of the subfield. Here we select and describe a few issues and recent publications that are most relevant to our new results, and then return to the result just described, i.e., our estimate of $\beta = 1.5$ at c=0 and its sweep-rate dependence.

The ABBM model [10] that yields the scaling functions Eqs. (3.3-3.5) is a single-degree-of-freedom model that neglects nucleation, interactions between DWs and temperature effects, and is valid in the limit of low disorder. It has been used as a basis for understanding the measured value $\beta = 1.5$ at low sweep rates for a broad range of (mostly bulk) materials (refer to Table 1 in Ref. 9 and notes accompanying the table for details).

A generalization of the ABBM model introduced by Cizeau, Zapperi, Durin, and Stanley [11] (CZDS) and studied by others [23] yields the same $c = 0$ limit scaling exponents

$$\beta = 2 - \frac{1}{\gamma} \tag{3.6}$$

$$\gamma = \frac{d+1}{2} \tag{3.7}$$

where the more sophisticated model allows consideration of the effects of dimensionality d. A system governed by an upper critical dimension $d = 3$ should yield $\gamma = 2,\ \beta = \frac{3}{2}$ as in the ABBM model; for $d = 2$ the exponents become $\gamma = \frac{3}{2},\ \beta = \frac{4}{3}$.

A number of bulk and thin-film systems studied have also yielded values of the BE jump-amplitude exponent β that appear to fall into the $d = 2$ universality class $\beta = \frac{4}{3} = 1.33$ (refer to Table 1 of Ref. 9). A few recent examples will be discussed later in this chapter.

Driving-rate effects [24] and dimensional crossover [25] have been studied theoretically in model systems that exhibit Barkhausen noise and avalanche behavior. The experimentally-observed [11] linear dependence of scaling exponent on sweep rate (Eqs. 3.3-3.5)) for systems having $d = 3$ yielding $\gamma = 2$ and $\beta = \frac{3}{2}$ is explained [24] as resulting from "small avalanches disappearing from the distributions due to being absorbed into larger ones." According to this view of sweep-dependent exponents, an exponent inequality relationship exists that prohibits sweep-rate dependencies for certain ranges of the value of universal scaling exponents. In other words, the adiabatic limit $(c \to 0)$ exponents are believed to govern finite-sweep-rate effects. Specifically for $\gamma < 2$, no sweep-rate dependence is expected. From Eqs. 3.6 and 3.7 with $d = 2$ yielding $\gamma = \frac{3}{2}$ and $\beta = \frac{4}{3}$, there should be no sweep-rate dependencies, whereas for $d = 3$, $\gamma = 2$ and $\beta = \frac{3}{2}$ sweep-rate scaling is allowed.

The exponent inequality rule suggests that crossover between universality classes is an important factor in considering sweep-rate dependencies in measured scaling exponents. Effects of dimensional crossover on scaling of avalanche distributions has been explored theoretically [25] based on the single-interface model. In this model jump-amplitude histograms, $\mathrm{P}(\Delta\mathrm{M})$, were obtained from simulations on an $L_x \times L_y \times \infty$ geometry "sample" in which the interface (DW) motion occurs along the infinite-length direction. Within these model simulations, the adiabatic limit exponent β for P(ΔM) distributions was found to vary from $\beta = 1.06$ for $d = 2(L_y << L_x)$ to $\beta = 1.28$ for $d = 3(L_y = L_x)$ representing different aspect ratios L_x / L_y for the DW cross section; significant variation of β was also found to occur as a function of the inverse size function $\sqrt{L_x L_y}$ that characterizes interface area. Based on these simulations, the cutoff function was also explored using an explicit (stretched exponential) form: $\mathrm{P}(\Delta\mathrm{M}) = (\Delta\mathrm{M})^{-\beta} e^{-(\Delta\mathrm{M}/\Delta\mathrm{M}_o)^\eta}$ where the simulations yielded fitted values for the exponent η falling in the range of 2.4-3.5 for about sixty sets of $L_x L_y$ parameters. The jump-size distribution exponents β for $d = 2$ and $d = 3$ obtained from the above model are in good agreement with corresponding results based on numerical simulations (in one, two, and three dimensions) using a nearest neighbor cellular automaton model [26] describing self-organized criticality which yield $\beta = 0.98$ for $d = 2$ and $\beta = 1.35$ for $d = 3$. This limited overview of a few existing analytical models and numerical simulations that address BN scaling exponent properties serves as a basis for a closer examination of our results and a few related experiments, the objective being to place all of the results in some perspective.

Within the framework of the above outline of selected theoretical considerations, we briefly comment on a few experimental determinations of the exponent β that are related to our results. Wiegman [9, 27] determined values of β for permalloy thin films covering a thickness range from 3000Å to 500Å using the induction pick-up coil method. The values are in the range $\beta \sim 1.4 - 1.6$ for film thickness from 3000 Å to below1000 Å, with much wider variation $\beta \sim$ 1.3-2.0 for films below 800Å thickness where the sensitivity limit of the method is approached. Wiegman's experiments appear to be the only existing systematic experimental attempt to explore dimensional crossover effects in permalloy thin films. While the measured values of β in the thickness range 3000-1000 Å are compatible with d=3, the large variations in β obtained for thickness below 800 Å do not permit a meaningful comparison with our results or with various d=2 or d=3 values.

Puppin [20] reported $P(\Delta M)$ measurements of 900Å thick Fe films based on magneto-optical techniques in which the spot size was varied from $20\mu m$ to $700\mu m$. By rescaling the measured distribution functions for various spot sizes to achieve a wide dynamic range of $P(\Delta M)$ vs ΔM, a value of $\beta \sim 1.1 \pm .05$ was obtained. Corresponding measurements for permalloy microstructures [28] ($20\mu m$ squares, 800Å thick) yielded $P(\Delta M)$ distributions that manifested strong finite-size effects at the cutoff region rendering accurate determination of β difficult. Weak manifestations of these effects were noted in relation to our discussion of Fig. 3.3. Corresponding measurements [20] on larger permalloy structures (to $320\mu m$, 1600 Å thick) permitted an estimate ($\beta \sim 1.2$) based on approximately 1/2 decade of $P(\Delta M)$ data excluding the cutoff region. More recently, Kim et. al. [29] determined $\beta \sim 1.33 \pm .05$ for Co films ranging in thickness from 50Å to 500Å. In these experiments, the microscope field-of-view was varied, and the measured distributions were rescaled, as in Puppin's [20] work, to obtain $P(\Delta M)$ over a wide range of ΔM.

It is interesting to note that the value $\beta \sim 1.1$ obtained by Puppin [20] is compatible with the nearest-neighbor two-dimensional atomaton model numerical simulations [26] of self-organized criticality (SOC) in 2-dimensions, and that the value $\beta \sim 1.33$ obtained by Kim et. al. [29] agree with the 2-dimensional CZDS model [11] (or with the SOC 3-dimensional numerical simulations). However, neither of these experiments addressed the field sweep-rate dependence, and the procedure of rescaling $P(\Delta M)$ distributions determined using different fields of view have been shown to measure a different critical exponent than what is used for comparison [9]. At this point it is not reasonable to draw any detailed conclusions regarding the nature of critical exponents in thin-film systems in relation to any of these models.

b. Additional Curve Fitting

The issues and results outlined in the previous subsection suggest a more detailed discussion of Fig. 3.3 and additional efforts to explore alternative interpretations of the scaling exponent result are in order. Two limitations of the experimental data account for the difficulty in obtaining accurate values of the exponent β: 1) the large statistical errors associated with the 3-4 points for large ΔM (cutoff region) resulting from relatively few events, and 2) the limited dynamic range of the "power-law" region that is accessible without rescaling data. In addition, very little is known about the behavior of $P(\Delta M)$ in the cutoff region, and assumptions must be adopted for curve-fitting exercises that include the cutoff region. It may be possible (but difficult) to significantly improve both experimental limits. Here we attempt to examine, as carefully as possible, the existing data.

It was possible to extend the plot of $P(\Delta M)$ vs ΔM measured at the 25 Oe/sec sweep rate by binning digital records, extending the total number of points from 26 to 41 (the effective dynamic range was improved about a factor of two from 20:1 to 50:1). Application of a power law fit to 36 of the 41 points (neglecting the last 3 points in the cutoff region) yielded $\beta = 1.28 \pm .02$. The difference in the two values of β obtained from the 38 point fit and 23 point fit is greater than the precision of either determination based on a least square analysis (Table 3.1). The 38 point fit is judged to be more accurate. We are now faced with a dilemma: the value of β judged to be most accurate for low sweep rates is not consistent with $\beta = 3/2$ (ABBM model [10]) and the exponent inequality relationship [24] which permits frequency-dependent scaling.

Unfortunately, it is not possible, based on the currently achievable sensitivity of our experiment, to improve the accuracy of higher sweep-rate values of β significantly. At higher sweep rates, the effective sampling rate must also be increased and the effective dwell time (that determines the number of photons detected to measure ΔM) decreases and the resulting statistical noise increases. This increase in noise limits the sensitivity to small BE jump amplitudes. Several experiments (discussed in a following subsection) were carried out using a more intense (50 mW solid state) laser on the same permalloy microstructure and on a continuous 300Å thick permalloy thin film. The Fig. 3.3A P(ΔM) plot represents our data set obtained using the solid state laser and slow sweep rate. These experiments yielded slight improvements in the sensitivity and an adiabatic value of β (β=1.33±0.01) in good agreement with the result β=1.28±0.02 (Fig. 2B with binning), and measured values of β that clearly manifest sweep-rate dependent scaling (discussed later in relation to Table 3.2).

To further explore the possible interpretations of experimentally-determined values of β based on the data presented in Fig. 3.3B-E, additional curve fitting exercises were carried out (including the cutoff region) guided by the numerical simulations of scaling exponents and dimensional crossover that included some simulations of the cutoff function [25]. These simulations yielded $\beta \sim 1$ for d=2 and $\beta = 1.35$ for d=3 with cutoff exponents η for the stretched exponential in the range 2.4-3.5. A preliminary survey of parameter space relevant to our data revealed that $\beta = 1$ resulted in poor fits for all $P(\Delta M)$ results except for the highest sweep rate dH/dt=6.3x10^4 Oe/sec and that cutoff parameters M_o~80 and η~10 yielded reasonable fits to the cutoff at all values of dH/dt. While the value of the cutoff parameter η required to fit our data is significantly larger (over a factor of 2) than the range of values suggested by numerical simulations, the value we chose ($\eta = 10$) permits a slightly better estimate of the power law exponents by providing a more accurate representation of data points near the cutoff region.

Having eliminated $\beta \sim 1$ at low sweep rates, (2d SOC case) we considered the following four possibilities with M_o=83 and η=10 fixed: 1) $\beta = 1.28$ for all sweep rates; 2) $\beta \sim 1.28$ for the lower sweep rates but $\beta = 1$ for the high sweep rate; 3) $\beta = 1.5$ for all sweep rates; and $\beta = 1.5$ for the lowest sweep rates but $\beta = 1$ for the high sweep rate. We note that there is no reason to assume that the same cutoff function parameters should apply to different sweep rates, but without some rationale for selecting different cutoff function parameters, the above assumption seems justified. Table 3.1 summarizes how well the simulations match the data based on least square fitting using the chi-square criteria. Figure 3.4 illustrates typical fits including the cutoff region. The primary conclusion is that reasonable fits to all four P(ΔM) vs. ΔM data sets (Fig. 3.3B–E) occur for either $\beta = 1.5$ or $\beta = 1.28$ as long as $\beta = 1$ is used at the highest sweep rate. We cannot reasonably account for all of the $P(\Delta M)$ distributions, especially for the larger jumps, unless sweep-rate dependent scaling of the exponent β is permitted and $\beta \sim 1$ is used at the highest sweep rate. Additional curve fitting exercises applied to Fig. 3.3B–E data were judged unlikely to provide a low sweep-rate value of β accurate enough to distinguish between d=2 and d=3 models or to resolve the dilemma emerging from the c-dependent $P(\Delta M)$ data. A definitive resolution of the issue regarding the relationship

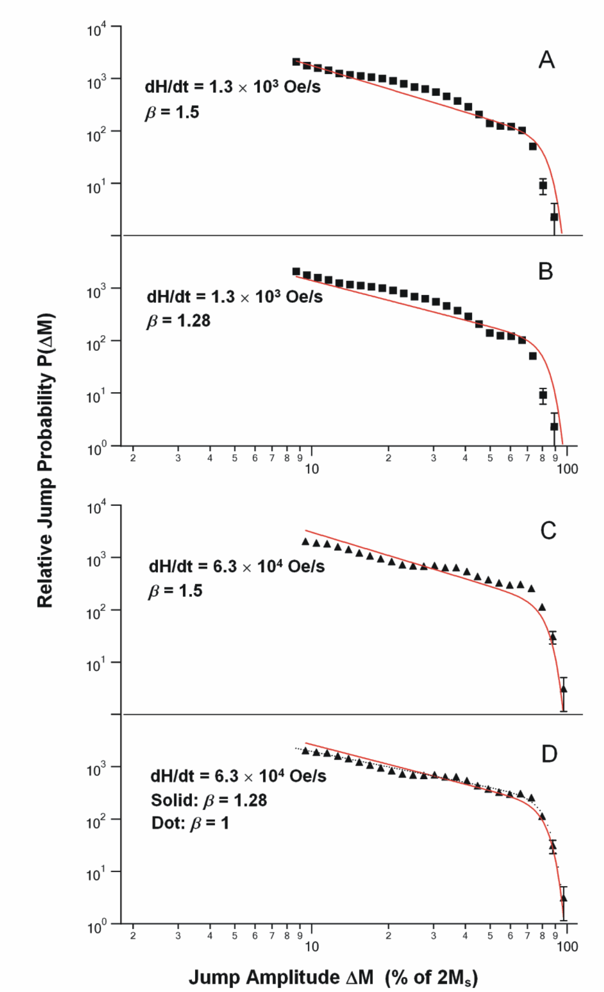

Figure 3.4 Log-log plots of relative jump probability $P(\Delta M)$ *vs. jump amplitude* ΔM *(same as Fig. 3.3) with different fitting procedures applied (refer to Table 3.1). Upper two panels display typical results obtained by fitting lower three sweep-rate* $P(\Delta M)$ *distributions based on the same cutoff parameters (Table 3.1) and (panel A)* $\beta = 1.5$ *or (panel B)* $\beta = 1.28$. *Lower two panels illustrate the problems of attempting to fit the high sweep-rate distribution using any exponent different from* $\beta \sim 1.0$. *A better fit to experimental points is possible with* $\beta \sim 1$

using a sharper cutoff function (this requires a value of η *larger than the range suggested by numerical simulations [25]).*

between sweep-rate dependent scaling of β and its c=0 value will require development of more sensitive experimental techniques and extensive experiments. Ideally one would like to: 1) explain in greater detail any effects on $P(\Delta M)$ resulting from microstructure size, 2) achieve lower statistical error in the cutoff region enabling a more accurate account of these effects on the power law extracted from the fits, and 3) achieve higher sensitivity at all sweep rates that would extend the $P(\Delta M)$ distributions far beyond the cutoff region allowing a more accurate evaluation of the power law exponent.

c. Additional Experiments/Sample-to-Sample Variation

In view of issues raised in the previous subsections, additional experiments were performed on a separate continuous 300Å thick permalloy film and on the same 200 x 200 $(\mu m)^2$ x 220 Å thick microstructure using a more intense 50 mW solid state laser. In these experiments, the data acquisition strategy was optimized to detect small BJs at the expense of not being able to accurately measure the DW velocity during a BJ. The P(•M) distribution obtained using the more intense laser (Fig. 3.3A) yield $\beta=1.33\pm.01$ at dH/dt=13 Oe/sec. This value of β is consistent with the result $\beta=1.28\pm0.02$ obtained using binning procedure described earlier applied to the data obtained at dH/dt=25 Oe/sec (Fig. 3.3B). Sweep-rate dependent studies of both the microstructure and continuous permalloy film yielded clear evidence of a sweep-rate dependent exponent having an adiabatic value $\beta\sim1.3$ that exhibited a strong sweep-rate variation to $\beta\sim1$ at higher sweep rates.

50mW Solid State Laser			
200 x 200 (μm)^2 Sample		Continuous Film	
Driving Rate	Beta	Driving Rate	Beta
13Oe/s*	1.33	0.9Oe/s	1.36
1.3 x 10^2	1.32	9	1.35
1.3 x 10^3	1.1	18	1.32
1.3 x 10^4	0.7	45	1.27
		67.5	1.22
		90	1.17
		112.5	1.11

*Data set shown in upper panel of Fig. 3.3

Table 3.2: Power law fits to independent data sets obtained using a more intense laser source and data reduction methodology that optimizes dynamic range (sensitivity) to ΔM rather than temporal resolution (which was emphasized in all other data sets presented in this chapter). Left columns, sweep rate and value of β obtained from P(ΔM) distributions for same 200 x 200 (μm)^2 microstructure used for other measurements (Figs. 3.2-3.4, Table 3.1); right column, corresponding results for a continuous (mm)^2 scale 300Å thick permalloy film. Note that for the continuous film the sweep-rate dependence of β is linear and that the departure of β from the adiabatic value occurs at a lower sweep rate for the thin film than for the microstructure film (because the jump durations are longer).

Table 3.2 displays the sweep-rate dependent values of β obtained using the more intense laser for both the continuous 300Å thick film and the 220Å thick 200 x 200 (μm)^2 microstructure. (These values of β do not correspond to the measured velocity distributions described later in Fig. 3.5 or to P(ΔM) distributions in Fig. 3.3 except for the top panel). A comprehensive account of these experiments that focus on sweep-rate dependent scaling and dimensional crossover is beyond the scope of this thesis. Based on the results presented in Tables 3.1 and 3.2 and in Figs. 3.3 and 3.4, we conclude the following regarding the exponent β for our permalloy films: 1) all data sets strongly support sweep-rate dependent scaling of β; 2) the most strongly supported value of β at low sweep rates (presumably the adiabatic limit) for permalloy films (and large microstructures) is $\beta=1.33\pm0.01$, which is compatible with the d=2 CZDS result $\beta=\frac{4}{3}$; 3) if the result $\beta=1.5$ (d=3) obtained by Wiegman for permalloy films having thickness in the 1000-3000Å range is valid, our results suggest dimensional crossover occurs in the thickness range between 1000 Å and 300 Å; and 4) Table 3.2 presents strong experimental evidence supporting (linear) sweep-rate dependence of β for adiabatic values of β significantly different from $\beta=3/2$.

d. Domain-Wall Velocity Distributions and Coercive Force Scaling

Figure 3.5 displays plots of DW velocity distributions obtained from M(t) transients (as described in Section 3.2) resulting from BJs at several sweep rates. These velocity distributions correspond to the P(ΔM) vs. ΔM results (except top panel data obtained using the 50 mW laser) presented in Fig. 3.3. Each point corresponds to the measured DW velocity associated with a BJ that occurred at the instant the applied field reached the value H. The scatter plots are a graphical representation of Eq. (3.2). The distributions terminate at H_{dm} (the constant geometry-dependent term), and the range of $H > H_{dm}$ where BJs are observed represent the statistical range of H_p values. The lower limit of DW velocity that can be determined is governed by the noise floor of the experiment. Digital signal averaging can be used to improve the signal-to-noise ratio

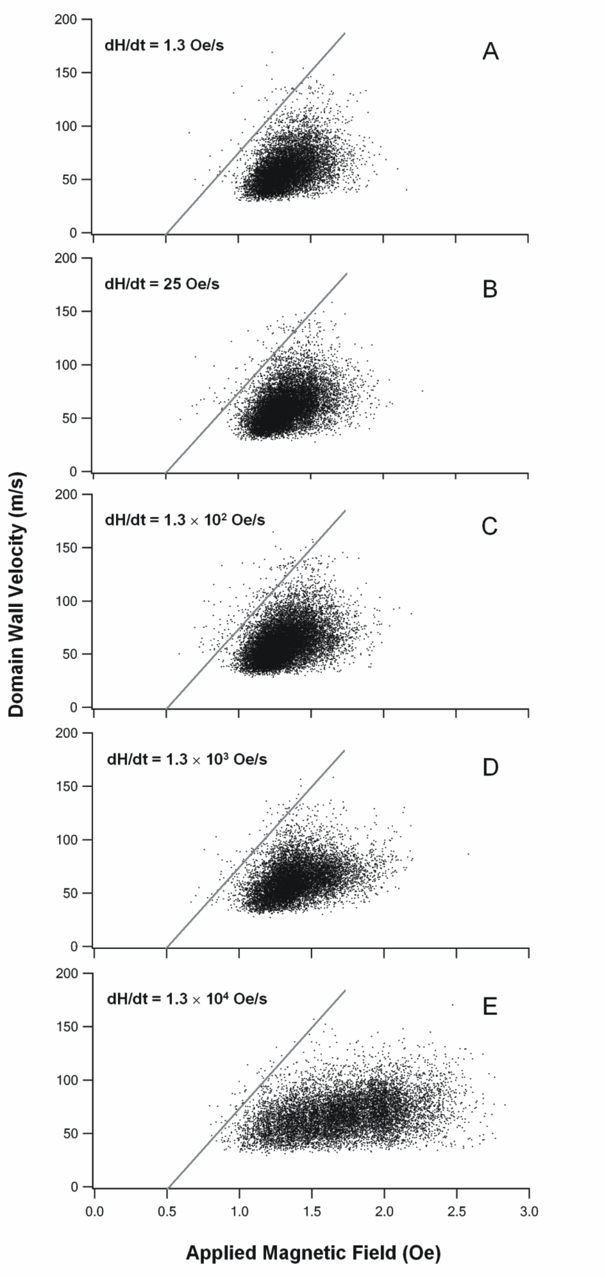

Figure 3.5 Domain-wall velocity and switching-field distributions associated with Barkhausen jumps as a function of drive-field sweep rate. Each point represents a DW velocity measurement (vertical scale) of a BE event that occurred at the applied field value (horizontal scale). Solid line, maximum estimated mobility $\dot{\zeta}_{\max}(H) \sim 150$ *m/secOe.*

thus lowering the noise floor (compare Fig. 3.2 A, B and C) but the temporal resolution is reduced. This procedure can be used to add points to the scatter plot (mostly at low velocities) but when this is done, it is necessary to keep track of previously recorded transients to avoid double counting which skews the distribution.

The maximum DW velocity that can be achieved during a BJ is governed by the mobility parameter ξ'_{max}. Wall mobilities have recently been theoretically studied in permalloy films and stripline structures based on direct integration of the LLG equations [30,31]. The simulated mobilities depend on both the film thickness and stripline width, an apparent manifestation of the effects of geometrical constraints on dynamic DW structure. In addition, detailed studies of DW mobility in nanometer scale wires (both experiments and numerical simulations) manifest field-dependent mobilities that suggest multiple DW propagation regimes [34, 35]. In the low field regime, the DW velocity is described by Eq. 3.1 with a nearly constant high value of ξ(~50m/sec Oe) that is consistent with the "Walker" solution of wall motion in a constant applied field. At a critical value of applied field H_w~4 Oe, the spin dynamics changes into a new regime characterized by negative differential mobility over a range of applied fields extending to ~25 Oe, after which a second constant mobility regime is established with a much lower value of ξ(~2.5m/sec Oe). The "Walker" regime mobilities are governed by the values of the gyromagnetic constant and damping parameter, α_G, used in the LLG simulation of spin dynamics. In the stripline simulations [31], an unrealistically high value of the damping parameter ($\alpha_G = 0.3$) was used to reduce computational time, resulting in low values of computed DW mobility. A realistic estimate of the intrinsic maximum mobility ξ'_{max} can be obtained from the theoretical mobility of a domain-wall, $\xi_t = \gamma\Delta/\alpha_G$, with characteristic wall width $\Delta_0 = \Delta/\pi$ with Δ defined in terms of the points where the magnetization direction crosses ± 90°. Using measured values of the gyromagnetic constant $\gamma = 0.0179$ Oe^{-1} nsec^{-1} [32] and $\alpha_G = 0.008$ [33] for permalloy thin-film structures and an estimate of $\Delta = 48$ nm for a Neél wall in a 31 nm thick film [30], $\xi'_{max} \sim 110$ m/secOe. The LLG simulations for 31 nm thick permalloy films (based on an assumed $\alpha_G = 0.05$) yield Neél wall mobility of 35 m/secOe; scaling this result assuming the measured value of α_G, ($\alpha_G = .008$) yields $\xi'_{max} > 200$ m/secOe. Based on these considerations, and on the apparent boundary of our experimental results, we assign $\xi'_{max} \sim 150$ m/secOe and indicate this limit on the scatter plots of Fig. 3.5 (solid lines with slope of ξ'_{max}).

The qualitative features of the DW velocity scatter plots (Fig. 3.5) are consistent with the ABBM model (as represented by Eq. (3.2)) and with general features associated with the stochastic nature of the model predictions including the $c \propto dH/dt$ dependent distribution functions (Fig. 3.3). The well-defined scatter plot boundaries are consistent with the intrinsic mobility limit governed by local damping (slope = ξ'_{max}), with the static coercivity of our permalloy sample, (intercept at 0.5 Oe), and with the noise floor of the experiment (minimum measurable velocity). The *averaged* velocities also appear to be consistent with prior measured mobilities ($\xi \sim 38$ m/secOe) of 30 nm thick permalloy films [34, 36] in the high mobility region. The jump amplitude distributions (Fig. 3.3) establish $c \sim 1$ at $dH/dt \sim 63$k Oe/sec, therefore the upper four panels of Fig. 3.5 correspond to $c << 1$, and the distributions are remarkably similar (especially the upper three). It is apparent that the transition $c \rightarrow 1$ is accompanied by a change in the velocity distribution (lower two panels, Fig. 3.5).

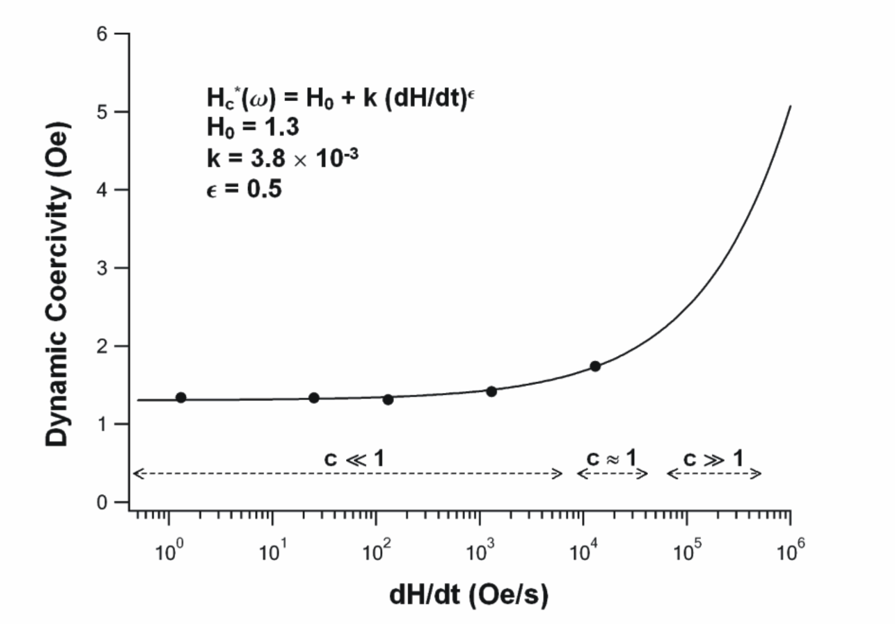

Figure 3.6: Frequency-dependent scaling of dynamic coercivity $H_c^*(\omega)$. Solid line scaling function for $H_c^*(\omega)$ determined from CW measurements (Ref. 15); points, average of H_p values from Fig. 3.4 for each value of parameter c.

Figure 3.6 establishes the compatibility of the measured BE distributions (Fig. 3.5) with multiple-loop averages that determine the sweep-rate dependence of the dynamic coercivity $H_c^*(\omega)$. This is important because later it is shown that the BE velocity distributions (Fig. 3.5) depart from the linear model of average DW velocity predicted by Eq. (3.1). In a recently reported study [15] of $H_c^*(\omega)$ for permalloy films and microstructures, we have shown that a frequency-dependent scaling function $H_c^*(\omega)$ under linear-ramp drive conditions can be obtained from a DW model adapted from Eq. (3.1):

$$H_c^*(\omega) = H_0 + k(dH/dt)^{\varepsilon}. \qquad (3.8)$$

Experimental data for $H_c*(\omega)$ obtained using a similar evaporated-film permalloy microstructure (100 x 150 $(\mu m)^2$ x 300 Å thick) follows this scaling function with k = 0.005 and $\varepsilon = 1/2$ for 1 • dH/dt • 10^9 Oe/sec (9 decades) with noticeable departure from the adiabatic limit $H_c*(\omega) \sim H_0$ occurring at about dH/dt ~ 10^4 Oe/sec. The solid line in Fig. 3.6 represents $H_c*(\omega)$ determined by multiple-loop averages over a very wide frequency range [15]. The five points plotted over the solid line represent averages of the five BJ distributions (Fig. 3.5) for each corresponding value of dH/dt. The agreement is excellent, showing that the averaged statistical data (BJ events at various H) obtained at a prescribed sweep rate reduce to the expected value of $H_c*(\omega)$. Note that the measured frequency dependence of the magnetic energy loss (which is proportional to H^*_c for square loops driven to saturation) proves that eddy-current damping, which scales as ω^2, is not important for the thin-film samples used in these experiments. The scaling law, Eq. (3.8), and the measured $H_c*(\omega)$ data represented in Fig. 3.6, and described in greater detail in Ref. 15, appears to be a general feature of thin-film magnetic response when eddy-current damping is suppressed provided that the $H_c*(\omega)$ measurements are carried out over a sufficiently broad frequency range [15, 36, 41].

Several features of the experimental results (Fig. 3.5) provide striking evidence of the limitations of Eq. (3.1) in describing DW motion beyond the adiabatic ($c \rightarrow 0$) limit. The statistical nature of switching for $c < 1$ is particularly evident in microstructures where $\Delta M/M$ can be large yielding very large fluctuations in the non-averaged DW velocities and switching fields. Also apparent from Fig. 3.5 is the departure of $<\upsilon(H - H_0)>$ from the linear dependence on H that is inherent in Eq. (3.1). Figure 3.7 displays plots of $<\upsilon(H)>$ obtained by averaging the measured velocity distributions around equally-spaced values of H in the region of $H > H_{dc}$. A significant departure from the linear relationship between ν and $(H - H_0)$ is observed for all drive-field ramps studied (Fig. 3.5) especially at the larger values of H_p, and higher values of dH/dt. A more accurate description of the experimental data for $<\upsilon(H)>$ obtained from averaging the measured distributions (Fig. 3.5) is obtained from the nonlinear version [9,15] of Eq. (3.1) that was used in obtaining the scaling function $H_c^*(\omega)$:

$$<\upsilon> = \xi(H - H_0)^q \tag{9}$$

with $\xi \sim \xi_{max}/2$ and $q = 0.27$ (Fig. 3.6B). Here we note that the form of the mobility equation given by Eq. (3.9) is used in descriptions of DW dynamics near a depinning transition [9].

The nonlinear dependence of $<\upsilon(H\text{-}H_0)>$ obtained by averaging the statistical velocity distributions is not a result of the sampling criteria used in generating the scatter plots (Fig. 3.5) from BJ data (Fig. 3.2). Similar nonlinear dependence was obtained by using velocity distributions resulting from BJs selected according to different ΔM criteria based on % change in ΔM relative to 100%: ΔM = 30-35, 40-45, 50-55 and 70-80 or using $\pi=1$. In addition we have found no evidence that adding the missing small BJs associated with the finite noise threshold in the measurement would substantially alter the averages that yield $H_c^*(\omega)$ or $<\upsilon(H)>$.

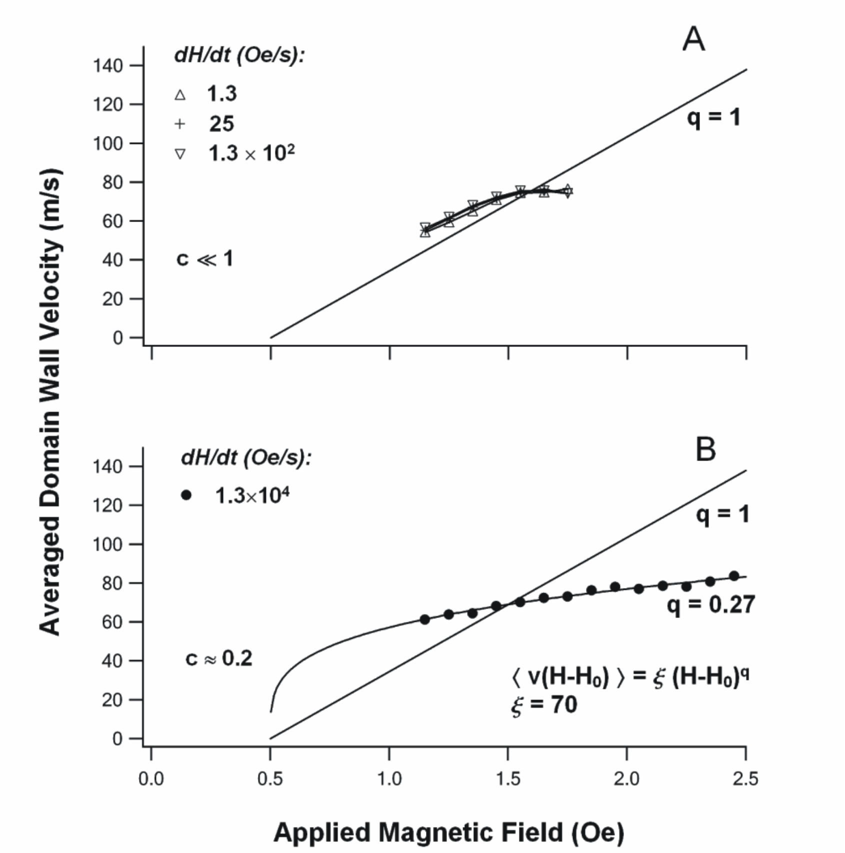

Figure 3.7: Averages of DW velocities vs. external field for two cases c << 1 (Panel A) and c ~ 0.2 (Panel B). Panel B displays two curves, a linear function (Eq. 3.1) and a nonlinear function (Eq. 3.7) fit to the <$\upsilon(H - H_0)$> data.

Departure of <υ(H)> from the linear model (Eq. (3.1)) is not unexpected. Computer simulation [31] of average DW motion in thin (300 Å) magnetic stripline structures predict mobility parameters (slope of <υ(H)>) that depart from linear behavior as H increases above H_0. These simulations were carried out using α_G ~ 0.3 (strong damping) compared to the more realistic α_G ~ 0.008 assumed for our permalloy samples. This accounts for the low values of calculated mobilities (~ 1 m/sec Oe). However, essentially all of the calculated υ(H) plots in Ref. 31 (and specifically the plot for 300 Å thick 5000 Å wide strip) can be fit by Eq. (3.7) with $q < 1$. The variation of mobility vs H is attributed to dynamic changes in DW structure at larger field values.

Experiments [34] that directly measure the mobility parameter ξ clearly show that the mobility is H dependent and exhibits dramatic negative differential behavior near H_w, the Walker breakdown field [34, 35]. This effect is relevant to frequency-dependent studies of DW velocities at constant applied field amplitude because at higher frequencies the switching (on average) occurs at higher values of H as shown by the distribution functions in Fig. 3.5, and the mobility parameter (slope of $\nu(H)$ curve) is no longer constant as H approaches H_w.

It is interesting to note that Monte Carlo simulation [42] of magnetization reversal in ultra-thin Fe/W(110) predict $\upsilon(H)$ behavior consistent with Eq. (3.7) but with $q > 1$. Specifically, for 1.5 ML films, the film consists of nanometer-scale 2 ML thick islands in a continuous 1 ML epitaxial film. In this system, thermal effects play a dominant role because the BJ volume is very small, and governed by the island size. Calculated M(t) results for this ultrathin film system manifest BJ behavior very similar to our Fig. 3.2 data; also, power scaling law of $H_c^*(\omega)$ is predicted, and the average calculated velocity (for 1.56 ML) films $<\upsilon(H)>$ can be fit by Eq. (3.7) with $q \sim 2$. Based on these considerations, it appears that the form of the mobility equation (Eq. (3.9)) is able to account for DW dynamics in many practical cases including ultrathin films and microstructural strips. In extreme limits, when H approaches or exceeds the Walker breakdown field, it is necessary to assume that the mobility ξ is strongly dependent n H.

3.4. Summary

In summary, this chapter presents the first (to our knowledge) direct measurements of BJ velocity distributions in the (thin film) limit where eddy-current damping is negligible. The measured velocity distributions are confined to a region of $\upsilon(H)$ space defined by a maximum DW mobility ξ'_{max} that is governed by local damping, and compatible with accepted measured parameters for permalloy.

The BJ amplitude distributions $P(\Delta M)$ vs. ΔM determined from our microstructured thin-film samples exhibit sweep-rate dependent power-law behavior with a sharp cutoff region similar to what has been observed in bulk materials where eddy-current damping governs DW velocities. Our microstructured samples are large enough to suppress significant departures from power-law behavior permitting estimates of the scaling exponents. Analysis of $P(\Delta M)$ distributions for four sweep-rates based on a uniformly applied power-law fitting criteria covering the same range of ΔM (that neglects the cutoff region) yields an estimate of $\beta \sim 1.5$ at low sweep rates with β decreasing to $\beta \sim 1$ at the highest accessible sweep rate of dH/dt=6.4 x 10^4 Oe/sec. This preliminary result is compatible with the ABBM model, with experimental results on a class of bulk samples, and with measurements of β in permalloy films over a thickness range extending from 3000Å to 500 Å. This interpretation based on a dataset having limited dynamic range is also compatible with the sweep-rate inequality relationship that permits sweep-rate dependent scaling for adiabatic values of $\beta = 3/2$.

It was possible to improve the sensitivity and therefore the dynamic range of the $P(\Delta M)$ distribution for the high temporal resolution measurements at the lowest drive frequency by binning M(t) sampling. The extended range of power-law behavior resulted in a more accurate (and lower) value of β in the adiabatic limit, $\beta = 1.28 \pm 0.02$. This value of β should not allow sweep-rate dependent scaling but all reasonable attempts to fit all four measured P(ΔM) distributions (Fig. 3.3B-E) obtained at high temporal resolution including reasonable account of cutoff regions failed to allow an interpretation that did not include sweep-rate dependence of β.

Additional experiments conducted on the microstructure and on a 300Å thick permalloy film using a more intense laser source (slightly better intrinsic dynamic range) yielded measured values of β in the range of $\beta \sim 1.33 \pm 0.01$ at low sweep rates, and clear evidence of sweep-rate dependent scaling (Table 3.2). We conclude that based on all of the results obtained on our permalloy microstructures and thin films to date, that the best estimate of β at low frequencies is $\beta = 1.33 \pm .01$, which is consistent with the CZDS model with d=2, and that sweep-rate dependent scaling is observed for all data sets independent of whether they favor d=3 (β=3/2) or d=2 ($\beta = \frac{4}{3}$) behavior.

Our results definitively rule out $\beta \sim 1$ at low sweep rates corresponding to SOC in d=2 which has been reported in other thin-film systems. The primary conclusion regarding the understanding of the BE in thin film materials, especially the scaling, and critical exponents, is that the understanding of these phenomena is very primitive, and that a large amount of systematic work will be required to resolve the apparent inconsistencies and discrepancies. There are reasonably good prospects of advancing the experimental methodology based on MOKE detection of BJ that will permit higher sensitivity measurements, which should allow more definitive interpretation.

Our measured velocity distributions are compatible with general features of the ABBM description of the BE (including the $c \rightarrow 0$ jump amplitude exponent for $P(\Delta M)$). Averaged values of H_p as a function of c (sweep rate) reproduce the frequency dependence of $H_c^*(\omega)$ reported in energy-loss scaling studies of permalloy microstructures. More specifically, the crossover point c ~ 1 determined from jump-amplitude distributions is associated with a significant change in the shape of the $\upsilon(H)$ scatter plots as well as the onset of more rapidly increasing energy loss scaling. In the $c >> 1$ limit, the distribution functions for $\upsilon(H)$ are believed to narrow and cluster around the line that defines the average mobility ξ and $H_c^*(\omega)$ [43]. It is clear from the distribution Fig. 3.3E corresponding to c ~ 0.2 that this trend has not begun to be manifested, nor is it apparent for c ~ 1. One point worth mentioning regarding the sweep dependence of the exponents (Eqs. (3.3-3.5)) is the role played by DW damping. Measurements of bulk samples where eddy-current damping limits mobility detect sweep-rate variation at relatively low sweep rates whereas our experiments on thin films require rather high sweep rates to detect significant departure of the measured exponent (β in this chapter) from the adiabatic limit value. This difference is probably a manifestation of the difference in DW velocities resulting from local (gyromagnetic) vs nonlocal (eddy-current) damping; therefore the relationship between the sweep-rate dependence of scaling exponents and the dominant DW damping mechanism is a subject that appears to merit additional attention. A final feature of these results is the departure of averaged stochastic velocities (Fig. 3.6, Eq. (3.7)) from the linear model Eq. (3.1). The results presented in this chapter clearly demonstrate the limitations of modeling magnetic switching based on a nonstatistical description, even in the sweep rate range where c ~ 1.

Chapter 4: Negative Barkhausen Jumps in Permalloy Thin-Film Microstructures

4.1 Introduction

Since their discovery, Barkhausen effects have been extensively studied [9] because they belong to an important class of nonlinear-dynamical phenomena that exhibit power-law distributions of jump sizes and durations characteristic of scale-invariant behavior [11, 45]. The universal stochastic behavior observed in low sweep-rate magnetic reversal can provide insight into related behavior associated with stock market fluctuations, earthquakes, material failure by fracture and other related phenomena.

In all Barkhausen jumps, the magnetic system experiences a transition between two different metastable states separated by an energy barrier. Most Barkhausen jumps (positive jumps) produce changes in local averaged magnetization that reduce the Zeeman energy $\langle M \bullet H \rangle_V$ within the jump volume, where the brackets represent an average of the scalar product of magnetization M and local magnetic field H over the jump volume. A succession of such jumps can eventually result in field-driven magnetization reversal. Negative Barkhausen jumps [46], in which changes in local magnetization oppose the applied field direction, have also been detected in several bulk materials using standard pickup coil technology [47-49] and, more recently, high-resolution magneto-optic techniques [50]. Figure 4.1 shows the pickup coil technology and a real signal from pickup coil measurement showing negative BJs. Negative Barkhausen jumps require a source of energy sufficient to overcome not only the local pinning potential, but also the increase in local Zeeman energy associated with the new local magnetic configuration that has magnetization opposing the applied field.

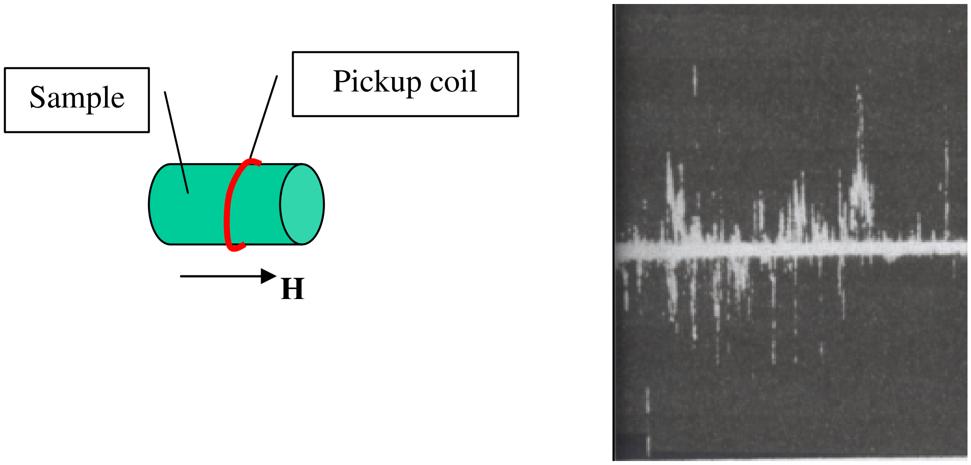

Figure 4.1: The pickup coil technology for detecting BN. Left panel: Experimental setup. Right panel: A real signal from pickup coil measurement [46], which shows both positive and negative Barkhausen jumps.

One source of energy that can drive negative Barkhausen jumps is thermal energy. A thermally-excited fluctuation in local magnetization can occur when thermal energy is comparable to the change in magnetic energy associated with a Barkhausen jump. Thermal effects are justifiably neglected in describing Barkhausen phenomena in bulk materials because the effective (Barkhausen) volumes are too small to produce measurable signals in most types of measurements [11]: the volume is given by:

$$(2\mu_o M_s H_p)\,\Delta V \sim kT$$

where H_p is the local pinning field, M_s, is the saturation magnetization, T is the temperature, and ΔV is the volume over which the magnetization reverses during a jump. Reasonable assumptions for parameters associated with soft magnetic materials lead to $\Delta V < 10^{-18} m^3$. Estimates of signals in inductive pick-up experiments corresponding to this jump volume fall far below the sensitivity limit of this technique. Thus any negative

Barkhausen jumps observed by pick-up coil experiments in bulk magnetic materials must result from a mechanism different from thermal excitation.

Negative Barkhausen jumps were first predicted in 1930 [47] and detected experimentally in 1951 [48]. The first experimental observation of negative Barkhausen jumps was carried out using a Fe-Si frame monocrystal [46]. This experiment was followed by experiments on annealed polycrystalline wires [49] and amorphous ribbons [50]. Some early work also explored the change in the surface domain structure of polycrystalline Fe-Si specimens by magneto-optic Kerr microscopy [51]. That work provided evidence of field-driven changes in domain configurations that could result in negative Barkhausen jumps.

The physical mechanisms responsible for negative Barkhausen jumps have not been clearly identified by prior work, although the experimental results offer several possibilities. Initial experiments revealed a strong correlation between the jump-size distributions of positive and negative Barkhausen jumps, leading to the conclusion that negative jumps were coupled with, and in some way dependent on, positive jumps. Experiments on polycrystalline samples revealed negative jumps when sufficiently high temporal resolution was used ($\Delta\tau \sim 1$ μsec) but failed to detect negative jumps with lower temporal resolution ($\Delta\tau \sim 100$ μsec). A model based on local-field coupling induced by eddy-currents [52] from positive jumps yielded estimates of local-field amplitudes ($H \sim 5 \times 10^3$ Oe) with risetimes ($\tau_r \sim 0.5$ μsec) that appear to account for the negative jump observations in bulk materials. Additional tests of the eddy-current coupling model in bulk materials based on the strong temperature-dependence of conductivity (and thus eddy-current coupling) were subsequently carried out that provided additional support for this mechanism [53]. The eddy-current model also seems to account for the fact that no negative jumps are observed in high resistivity ferrite materials [54].

The most recent study of negative Barkhausen jumps compared experimental results obtained from an amorphous Fe-Ni based alloy ribbon (Fe_{63} B_{14} Si_8 Ni_{15}) using both the traditional inductive pick-up coil tchnique and a new high-spatial resolution magneto-optic Kerr effect (MOKE) polarimeter [50]. Statistical distributions of positive and negative jump amplitudes obtained from the pick-up coil measurements (over three-decade dynamic range) and from a 50 μm-resolution magneto-optic investigation (about one decade dynamic range) yielded the same (jump amplitude) power-law exponent: $\alpha = 1.6$. This result is a strong indication of scale invariance of both positive and negative Barkhausen jump distribution functions in the amorphous ribbon system, and a good indication that the negative jumps are coupled to positive jumps. Probing the sample surface at 50 μm spatial resolution using the MOKE technique revealed surface regions where negative jumps were produced, and other regions where no negative jumps were produced. One puzzling feature of the inductive pick-up data is the appearance of isolated negative Barkhausen jumps that seem to be inconsistent with the eddy-current mechanism, thus suggesting an alternative mechanism may be required to explain all observed negative Barkhausen jump effects.

This chapter describes experiments (published at Journal of Applied Physics [86]) in which negative Barkhausen jumps are studied in thin-film Permalloy microstructures. Magneitzation reversal was simultaneously probed globally and locally with high temporal resolution using a novel dual-beam magneto-optic technique. The film thickness is 50 nm, which is thin enough to suppress eddy-current effects (even in high-conductivity materials) due to thickness scaling of these effects [15, 17]. The simultaneous measurement of positive and negative Barkhausen jumps at high (≈ 0.1 μsec) temporal resolution and sequential magnetic force microscopy (MFM) images of the same microstructure provides the basis for postulating a new mechanism for producing negative Barkhausen jumps in thin films (that is also present in bulk materials).

4.2 Experiment

Figure 4.2 shows a schematic representation of the dual-beam MOKE polarimeter. Two lasers are used: a 50 mW solid-state laser (λ = 658 nm) and a 20 mW He-Ne laser (λ = 632.8 nm). Each laser is part of a separate high-sensitivity, high-spatial resolution polarimeter similar to the instrument (previously described) that was used to study domain-wall dynamics and Barkhausen effects in Permalloy microstructures

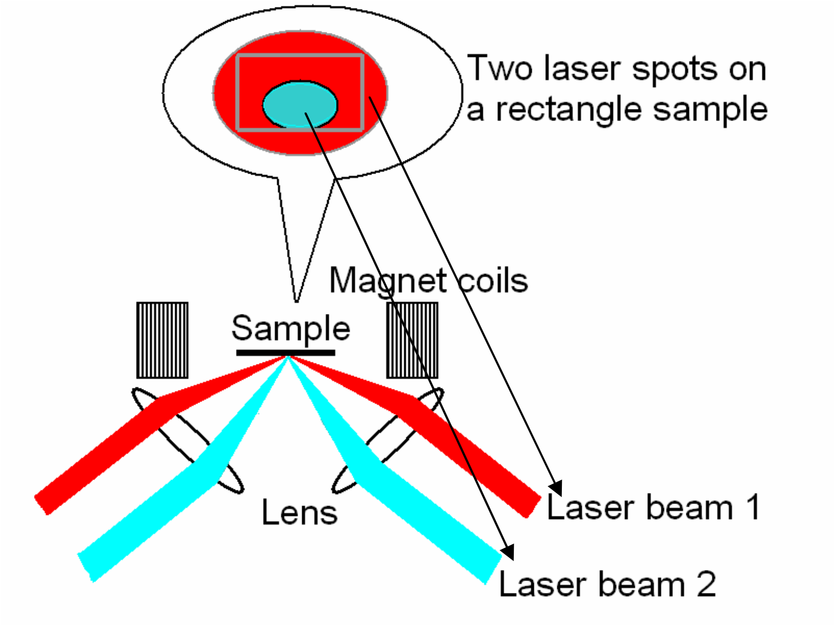

Figure 4.2 Schematic diagram of dual-beam MOKE experiment

Beam expanders, objective lenses, and other optics allow the two beams to be focused on the microstructured sample with overlapping but independently-selected spot sizes. The 45° incident angle provides elliptical beam profiles with minimum spot size (long axis) of 20 μm. Each polarimeter achieved (amplifier bandwidth limited) temporal resolution of approximately 0.1 μsec, and a signal-to-noise ratio of approximately 5:1 at a sampling time of 0.1 μsec/sample. Slightly higher sensitivity was achieved for the smaller spot channel (λ = 658 nm) used to probe negative jumps due to its higher laser power. Both polarimeters were configured to measure the longitudinal MOKE which is sensitive to the magnetization parallel to the x-direction applied field (M_x) averaged over the illuminated sample area.

Six rectangular Permalloy microstructures were fabricated using standard e-beam lithography/lift-off techniques. Three microstructures were 100 μm × 70 μm; the other three were 50 μm × 36 μm. All six structures were fabricated on a thermally-oxidized Si(100)-substrate. The film (thickness ~ 50 nm) was grown by e-beam evaporation at a pressure of 4×10^{-9} Torr. Sequential magnetic force microscope (MFM) images of the microstructure domain patterns were obtained using the AFM/MFM with Helmholtz coils adapted to provide a magnetic field. Several dozen MFM images and over 6000 MOKE switching loops were measured in the experiment.

4.3 Results and Discussion

Figure 4.3 displays typical hysteresis loops measured using the dual-beam MOKE polarimeter. The applied field was a linear ramp (triangle wave) at a frequency of 1.25 Hz. The effective sampling time for data presented in Fig. 2 was 0.5 msec (each loop contains 1600 points) which accounts for the high signal-to-noise ratio. The upper panels correspond to the smaller-diameter beam (20 μm); the lower panels correspond to the larger-diameter beam (the larger-beam diameter 1/e width was adjusted to be approximately equal to the microstructure width). Therefore, the larger beam probed all

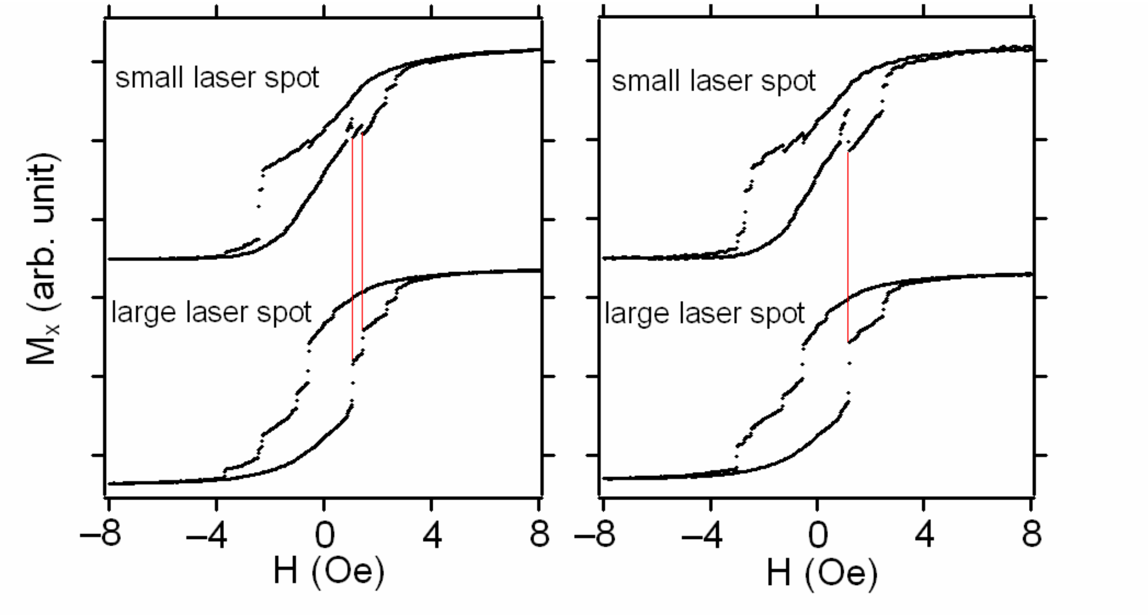

Figure 4.3 Typical hysteresis loops obtained from large laser spot (full area of microstructure) and small lasers spot (~20% of sample area) showing negative Barkhausen jumps from smaller region correlated with positive Barkhausen jumps from entire sample.

Barkhausen jumps produced by the microstructure within the sensitivity limit; the smaller beam probed below 20% of the microstructure area. Analysis of over 6000 dual-beam hysteresis loops resulted in the following qualitative characteristics of positive and negative Barkhausen events in the thin-film Permalloy microstructures: 1) negative jumps were observed only in the smaller spot channel; 2) every negative jump was correlated with a positive jump; 3) all negative jumps were smaller than the corresponding positive jumps; 4) negative jumps occurred at a rate of approximately 20% of positive jump production, and the rate of negative jump production was sensitive to the location of the smaller beam on the sample.

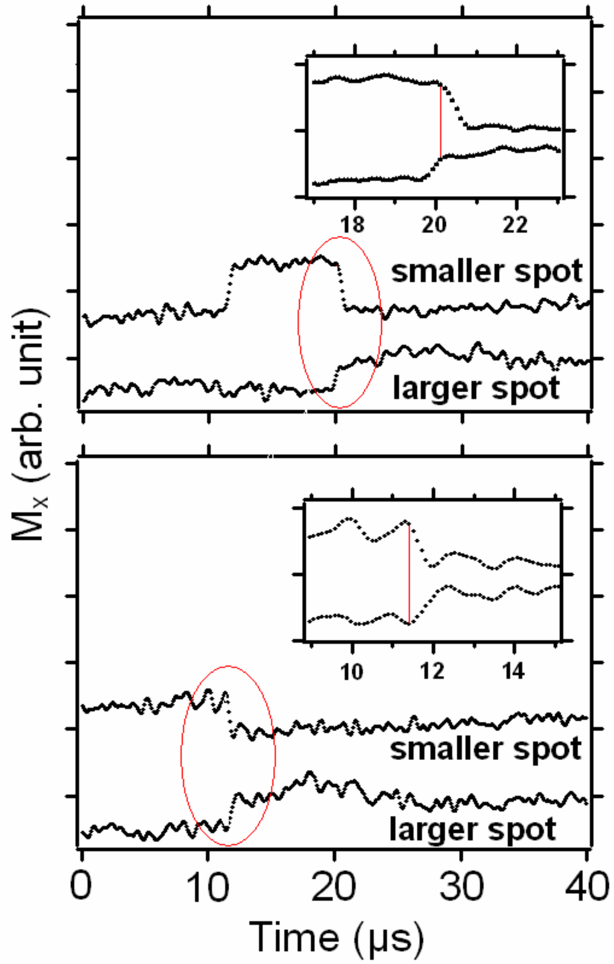

Figure 4.4 High temporal resolution time record of spatially-resolved magnetization from small region (upper traces of both panels) showing negative Barkhausen jumps correlated with positive Barkhausen jumps from full area of microstructure. Each point corresponds to a 0.1µsec sample. Upper panel with expanded-scale insert shows negative jump occurring at the end of positive jump (time delay approximately 0.5 µsec). Lower panel shows negative jump occurring at leading edge of positive jump (no time delay).

Figure 4.4 displays portions of a dual-channel magnetization measurement at high temporal resolution (0.1 μsec/sample). The instrumentation noise floor is apparent at the short integration time interval (compare noise of $M_x(t)$ data in Fig. 4.3 and in Fig. 4.4). Barkhausen jumps are clearly resolved, and the specific events displayed in the two panels were selected to demonstrate evidence of measurable time delays in the jump dynamics. The lower panel corresponds to an event where the positive jump and negative jump occur simultaneously within the temporal resolution of the measurement. The upper panel corresponds to an event where the negative jump is not triggered until after most of the ΔM associated with the positive jump has occurred (a 0.5 μsec delay). The upper panel also shows an event in which the negative jump was preceded by a positive jump (10 μsec). The difference in sensitivity of the two channels resulting from the difference in probed area results in the amplitude of the positive jump in the large beam area channel being obscured by the noise floor.

Time delays of several tenths of a microsecond (as shown in Fig. 4.4 upper panel) can be reconciled with the proposed new mechanism for negative-Barkhausen jump production based on field-driven configurational changes in domain patterns and the domain-wall velocities associated with wall displacement. Jump size distributions are discussed later (Fig. 4.5). Positive jump sizes range from values corresponding to approximately half of the total sample volume to below the sensitivity limit; the largest negative jump sizes are at least a factor of 10 smaller. Typical domain-wall velocities can be estimated from the fractional change in magnetization of a positive jump and the time required for the jump to occur as described previously. Typical domain-wall velocities during a Barkhausen jump are $\upsilon \sim 50$ m/sec, and typical jump execution times (Fig. 3) are $\Delta\tau \sim 1$ μsec (for a large jump). Negative jump time delays of several tenths of a microsecond to a microsecond following the initiation of a positive jump can be accounted for based on the jump execution time. If a negative jump event is stimulated at the initial location of a domain-wall that produces a positive jump, the negative jump will be simultaneous with the positive jump. However, if the negative jump results from a configurational change of the domain structure that is not stimulated until near the end of a positive jump, there must be a time delay equal to the positive jump execution time which is subject to the domain-wall velocity and jump size.

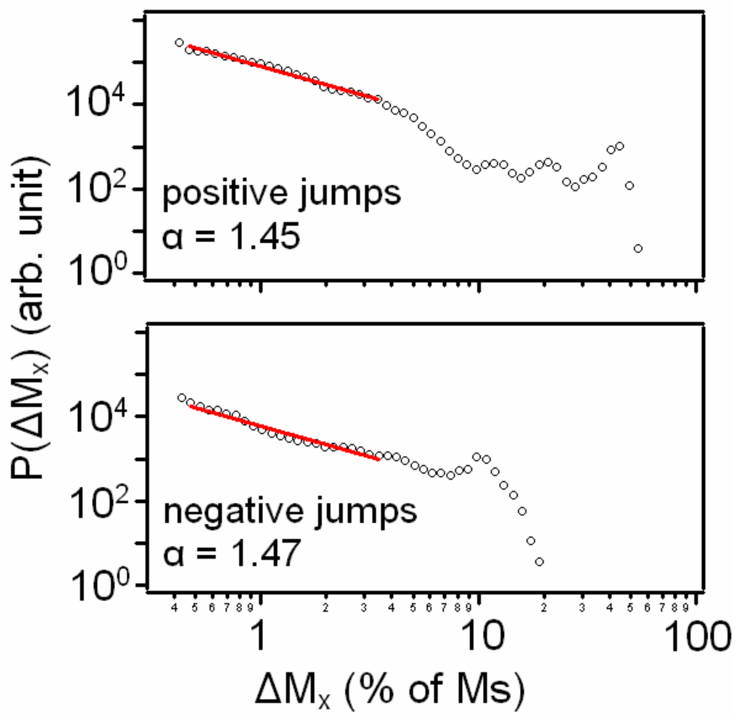

Figure 4.5: Log-log plots of probability distribution $P(\Delta M_x)$ versus jump size ΔM_x for positive and negative Barkhausen jumps. The unit of ΔM_x is percent of saturation magnetization of the sample. Cutoff behavior and non-uniform power-law scaling of large ΔM_x result from relatively small numbers of allowed domain

configurations; at smaller ΔM_x scales, both positive and negative distributions exhibit power-law behavior characterized similar exponents (straight line).

Figure 4.5 displays log-log plots of probability distributions as a function of jump size for positive and negative Barkhausen jumps. Both distributions manifest cut-off behavior associated with the sample size (large beam, positive jumps) or the beam size (small beam, negative jumps) as well as structure for large jump amplitudes attributed to the relatively small number of domain configurations that can be achieved in a microstructured thin film sample (breakdown of power-law scaling resulting from finite size effects) [20, 28]. Jump size distributions for smaller values of ΔM_x (for both positive and negative jumps) show evidence of the uniform power-law scaling observed in jump-size probability distributions in bulk [11] and larger area thin-film samples [50]. The straight lines in Fig. 4.5 correspond to power law fits in the small jump-size regions, where finite-size effects do not disrupt the power-law behavior. The positive and negative jump-size distributions are very similar in this region, and are described by scaling exponents of 1.45 and 1.47, respectively. This observation suggests a correlation between the two processes.

Figure 4.6 displays a sequence of MFM domain images obtained during a slow linear-ramp-driven magnetization reversal cycle of one of the microstructures. Drawings that show more clearly the location of domain-walls are presented to the right with an elliptical outline that simulates a possible location of a local MOKE probe. Suggested spin directions corresponding to the various domains are indicated in the schematic drawing. The dotted lines indicate cross-tie structures [55, 56]. The lower panel displays $\langle M_x \rangle$ obtained by numerical averaging of the entire sample and $\langle M_x \rangle$ for the elliptical region, simulating a dual-beam measurement of the spatially-resolved magnetization of

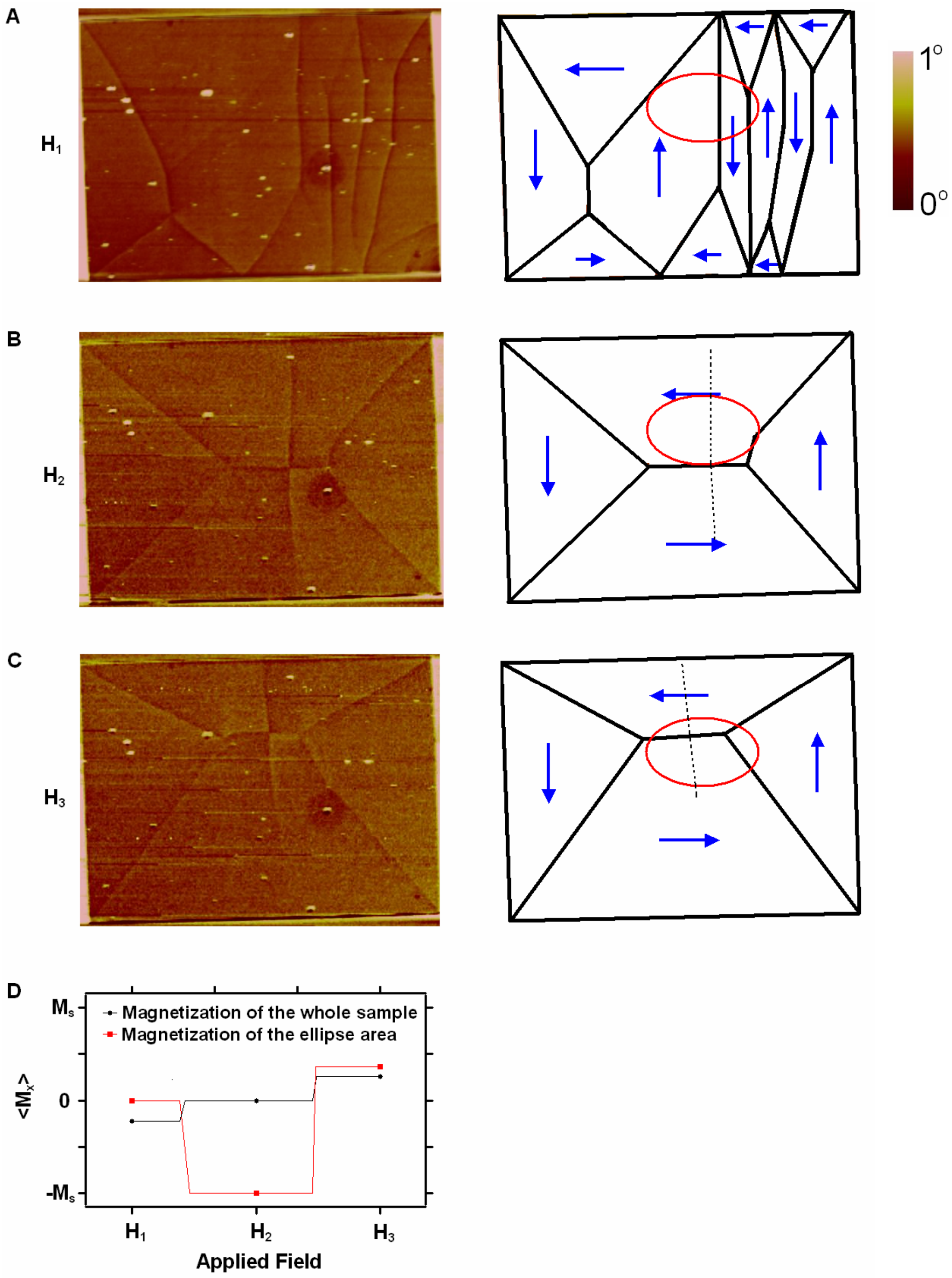

Figure 4.6 Three left-side panels: sequential MFM images of microstructure(50μm×36μm) domain-walls as applied magnetic field is increased

in discrete increments. Three right-side panels: schematic diagrams of MFM images with suggested spin orientation within each domain. Ellipse represents a region of the sample that, if probed by the dual-beam MOKE polarimeter, would yield a negative Barkhausen jump between panels A and B. Dotted lines indicate cross-tie structure. Lower panel: magnetization of entire sample (square) and of region enclosed in ellipse (circle), (as fraction of M_s *enclosed in areas) obtained by numerical average of* M_x *over the spin configurations. The red curve shows a negative Barkhausen jump between the* H_1 *and* H_2 *domain configurations.*

the three domain configurations. This simulation of a dual-beam MOKE measurement demonstrates how a configurational change of domain structure probed at a selected region of an actual microstructured sample can manifest a negative Barkhausen jump (small region) resulting from a larger (full sample) positive jump.

4.4 Conclusion

Dual-beam high-resolution magneto-optic Kerr effect polarimetry and magnetic force microscopy (MFM) are used to study negative Barkhausen jumps in thin-film Permalloy microstructures. The films are thin enough to suppress eddy-current effects and the measured Barkhausen volumes associated with negative jumps are too large to be attributed to thermal excitation effects. A mechanism that is independent of eddy-current and thermal activation effects is proposed to account for the negative Barkhausen jumps: configurational changes in domain-wall patterns in which a positive Barkhausen jump drives a region of the sample in a manner that results in an increase in local magnetization opposed to the drive-field direction. These configurational changes are driven by the Zeeman energy, but require the complicated local pinning potentials and anisotropy energies found in all practical magnetic specimens. Time delays of several tenths of a microsecond are observed in the coupled negative jump dynamics and these are compatible with the measured wall velocities and the feature of the mechanism that allows a negative jump to occur at any time during the driving positive jump event.

Chapter 5: Spin-Transfer-Torque-Driven DW Dynamics in Permalloy Nanowires

5.1 Introduction

Manipulation of spin distributions on a submicron scale plays a central role in data storage devices, and also offers new opportunities for future electronics technology [1, 57, 58]] termed "spintronics." The conventional way to switch a magnet is by applying a magnetic field. Recent experiments have shown that spin-polarized current can move a domain-wall. Compared with the field-driven method, using an all-electrical device where a spin-polarised current performs the magnetic switching has many advantages. It is easy to confine a current to a single device, allowing high device density and higher efficiency. Figure 5.1 shows the principle of spin-transfer-torque-driven domain-wall motion.

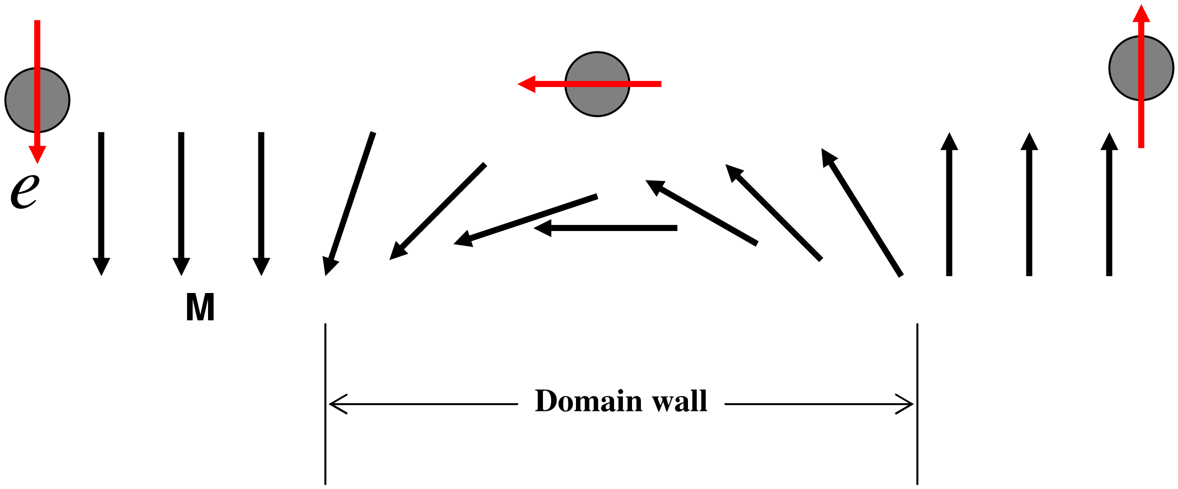

Figure 5.1: Schematic diagram showing spin-transfer-torque-driven domain-wall motion.

When spin-polarized electrons flow through a domain-wall, their spin momentum is transferred to the wall. If the current density is large enough, the domain-wall can be depinned and propelled in the direction of electron flow.

Recent theoretical [59-65] and experimental [66-70] work has addressed the underlying physical basis of magnetic domain-wall (DW) manipulation by electric current. While these studies have advanced the understanding of current-driven DW phenomena beyond the pioneering work of Berger [71-73] and others, there remain striking discrepancies between experiments and corresponding results obtained from existing phenomenological models and numerical simulations.

Specific discrepancies can be found in studies of pulsed electric-current-driven DW motion in thin-film-based Permalloy nanowires. The nanowire structures are small enough to permit numerical simulation of DW dynamics based on solving the modified LLG equation [60-64]. These model (one-dimensional) systems are ideal for exploring both magnetic-field- [34, 58, 74,] and electric-current-driven [66-69] DW dynamics.

Recent experiments on field-only-driven DW dynamics [34] have yielded results in essential agreement with phenomenological descriptions and numerical simulations [75]. To account for the effects of electric current, two terms have been added to the LLG equation [61], which correspond to “adiabatic”[59-64] and “non-adiabatic”[59, 61, 68, 72] spin-transfer torques, as shown in Equation (5.1)

$$\frac{\partial \vec{M}}{\partial t} = -\gamma \vec{M} \times \vec{H}_{eff} + \frac{\alpha}{M_s} \vec{M} \times \frac{\partial \vec{M}}{\partial t} \underbrace{- \frac{b_j}{M_s^2} \vec{M} \times (\vec{M} \times \frac{\partial \vec{M}}{\partial x})}_{\text{adiabatic}} \underbrace{- \frac{c_j}{M_s} \vec{M} \times \frac{\partial \vec{M}}{\partial x}}_{\text{non-adiabatic}} \qquad (5.1)$$

The spin-transfer-torque mechanism, which drives DW distortion and propagation, is described by a velocity parameter [60, 63], $b_j = P\, j\, \mu_B/(eM_s)$ and a spin-flip efficiency parameter $\in = v/b_j$ that is equivalent to the ratio of displaced DW spins flipped per polarized conduction electron. The symbols correspond to j = current density, μ_B = Bohr magneton, e = electronic charge, v = DW velocity; and for Permalloy, typical parameters for the conduction electron polarization P and saturation magnetization M_s are respectively 0.5 and 8.0×10^5 A/m^2. Theoretical models [61-63] of adiabatic current-driven DW displacements and velocities in Permalloy nanowire structures (assuming Gilbert damping) at $j = 10 \times 10^{12}$ A/m^2 (below $j_{cr} \sim 10^{14}$ A/m^2, the theoretical threshold for sustained motion) predict initial velocities v_{max} = 400 m/sec that decay to about 100 m/sec after 0.5 nsec (and essentially to zero after 2 nsec), with corresponding total displacements of $\Delta x \cong 150$nm. Under these conditions, the maximum spin-flip efficiency (which occurs at t = 0 when the current step is applied) is $\in_{max} = eM_s/P\mu_B\ (v_{max}/j) = 2.76 \times 10^{10}\ (v_{max}/j) \approx 1$, a value consistent with the assumption that conduction electron spins follow the local magnetization within the DW and transfer all of their spin momentum to the displaced wall. Analytical models of adiabatic current-driven DW motion [59] appear to be generally consistent with the results of LLG simulations summarized above. A recent theoretical analysis [76] of spin-transfer-driven DW dynamics that assumes Landau-Lifschitz damping predicts qualitatively different time-dependent displacements: sustained motion characterized by b_j.

Recent experiments [77, 78] that explore dc-current-driven enhancement of field-driven DW motion in Permalloy nanowires verify the existence of a steady-state current-driven force in the presence of an applied magnetic field. The velocity enhancements (v ~ 35 m/s at $j = 6 \times 10^{11}$ A/m^2) and corresponding high values of spin-flip efficiency $\in \sim 0.7$) are comparable with terminal velocities estimated from non-adiabatic corrections [61] to the adiabatic term in the LLG equations. The corresponding situation for pulse-current-driven DW displacements in Permalloy nanowires in the absence of an applied magnetic field is less clear.

Existing experimental estimates of current-driven DW velocities and spin-flip efficiencies have been based primarily on observation of pulse-driven DW displacements, Δx, using magnetic force microscopy (MFM) [66, 67]. Temporal resolution is achieved by using short-duration pulses to drive the DW and the (average) wall velocity is calculated by assuming that $\dot{v} = \Delta x$ / (pulse duration). The experiments have yielded estimates of prompt current-driven DW velocities in Permalloy nanowires ranging from 0.4 – 4 m/sec and spin-flip efficiencies of $\in < 0.1$ at current densities of $\sim 7 \times 10^{11}$ A/m^2 using pulse duration of 0.3 ~ 5.0 μs. These values of v and $\in$ are at least a factor of 10 lower than theoretical estimates [60, 63, 64]. The discrepancies have been attributed to dissipation of spin-polarized-current angular momentum by spin-wave creation associated with DW depinning [59]. Additional features of selected experimental results are that the measured DW displacements are observed to be proportional to the pulse duration [66] and dependent on pulse risetime [69]. This behavior is inconsistent with the prompt dynamics based on the adiabatic spin-torque mechanism [60, 63, 64]. Some of the discrepancies between experiments and (adiabatic term) theoretical predictions could be explained by non-adiabatic corrections to the spin-torque mechanism, however, recent evaluation of the spin-transfer-torque terms by Xiao, Zangwill and Stiles [65] casts doubt on the existence of a significant non-adiabatic contribution to the torque term at zero field proposed by Zhang and Li [61]. We note other experiments [70] that report the wall displacement does not depend on pulse duration, and that most measurements [66, 67, 70] of pulse-current-driven DW displacements obtain values ($x \sim$ several μm) considerably larger than those predicted based on the adiabatic mechanism ($x \sim 100$ nm)[60, 63]. All of these results suggest the need for more precise measurements of pulse-current-driven DW phenomena with sufficiently high temporal resolution to reveal the DW dynamics, at least on a short time scale compared to the pulse duration.

5.2 Experiment

The experiment reported in this chapter (published at Physical Review B [87]) overcomes some of the limitations of prior measurements of electric-current-driven DW displacement by using high-temporal-resolution magneto-optic Kerr effect (MOKE) tracking of the motion. While our new experimental results do not appear fully compatible with existing models of current-driven DW motion, the results are interpreted within the framework of the adiabatic and non-adiabatic spin-transfer torque mechanism. The new experiments manifest DW displacements that are proportional to current density for $j > j_t$ (experimental threshold current required to depin the DW) and independent of pulse duration for pulses longer than the intrinsic time resolution of the experiment (0.3μs). The experiments determine estimates of averaged current-driven DW velocities (as high as $v \geq 15$ m/sec at $j = 4 \times 10^{11}$ A/m^2) and high spin-flip efficiencies ($\in \sim 1$) that are consistent with the transient DW motion predicted theoretically for adiabatic-torque-driven wall motion. The factor-of-ten higher measured current-driven velocities and spin-flip efficiencies determined by our experiment show that pinning effects do not necessarily absorb most of the available spin angular momentum in current pulses having amplitude sufficiently above a threshold value.

Figure 5.2 illustrates essential features of the experiments. The 30nm-thick, 500nm-wide Permalloy microstructure was fabricated on an oxide-coated Si(100) wafer by e-beam lithography. Two orthogonal electromagnets allow application of B-fields parallel to the orthogonal nanowire sections to prepare a stationary (vortex structure)[79, 80] DW within the field-of-view of the MOKE polarimeter.

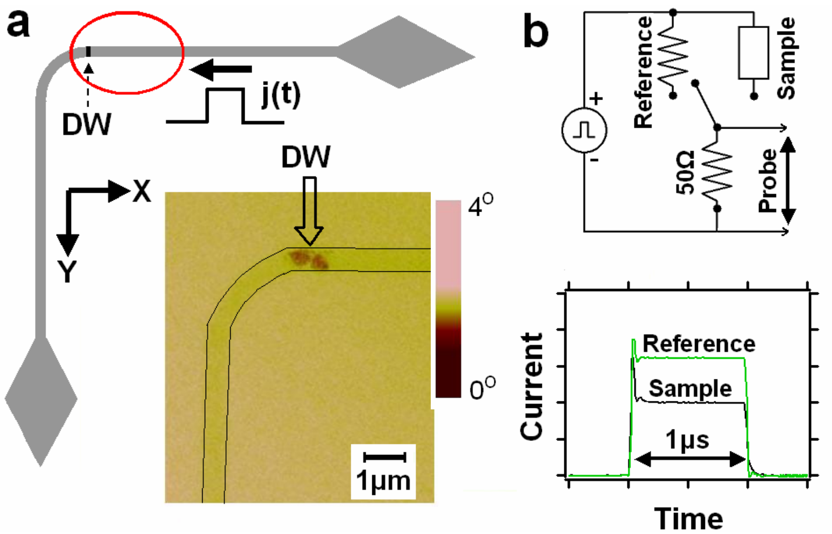

Figure 5.2: Panel a: schematic of Permalloy microstructure. Ellipse enclosing a DW indicates 1/e intensity profile of focused laser beam. Insert MFM image of the microstructure showing an injected vortex DW (the two lines are drawn by hands). Panel b: pulse-current measurement (100MHz sampling rate) of microstructure resistance R(t) that establishes the temperature rise due to ohmic heating.

The polarimeter utilizes a solid-state laser incident at 45° with s-polarization focused on a 10 μm spot (1/e width, major axis) at the wafer surface. The detected (longitudinal configuration) MOKE signal is proportional to the net magnetization $\langle M(x,t) \rangle$ of the microstructure (weighted by the beam intensity profile over the field-of-view). The polarimeter achieves temporal resolution of approximately 0.3 μs (pre-amplifier bandwidth-limited rise time), and the well-defined geometry of the experiment (including the feature that the DW width << beam diameter) permits accurate time-resolved measurements of DW displacements. The sample temperature was determined by high temporal resolution measurements of the microstructure resistance (R = 2.24kΩ at 300K) using calibration data for Permalloy reported by Yamaguchi [67]. Figure 5.2

displays the current response to voltage step functions (rise time t_r ~ 10 nsec) applied to a 2.24kΩ carbon resistor and to the microstructure. The thermal relaxation time is approximately $\tau \approx 50$ nsec. The sample temperature increases from 300K to 630K (in about 50 nsec) at $j = 4 \times 10^{11}$ A/m^2 corresponding to a 25% reduction in M_s ($T_c = 820$K for Permalloy)[81].

5.3 Results and discussion

Figure 5.3 displays a typical time-resolved measurement of electric-current-induced DW displacement for a pulse having $t_r \approx \tau$. Each point corresponds to a 0.1 μsec sample of the magnetization $\langle M(x, t) \rangle$. Head-to-head or tail-to-tail DWs are prepared as shown in the MFM image (Fig. 5.2). The prepared DW is then subjected (with B = 0) to an applied current pulse resulting in a DW displacement in the direction of electron flow. The DW position within the MOKE polarimeter field-of-view is related to the detected MOKE intensity by an error function erf(x) due to the Gaussian laser beam profile.

The location of the DW after pulsed B-field stimulated injection and its displacement after application of a current pulse having current density above j_t are both affected by pinning potentials in the nanowire. The 90^o bend functions like an engineered pinning center in the sense that the position of the injected DW is quite repeatable.

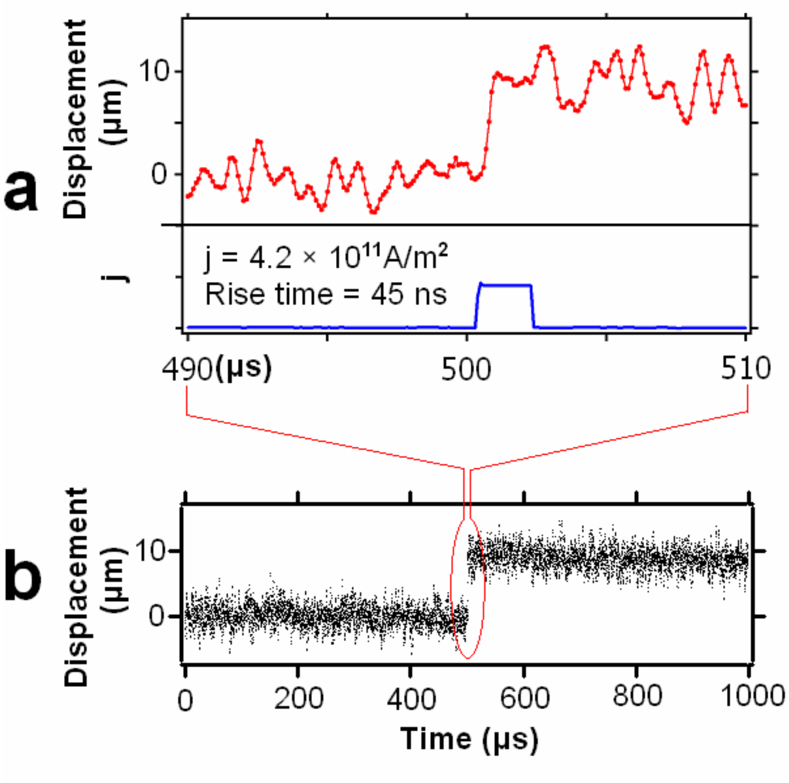

Figure 5.3: Panels a and b: high temporal resolution (0.1 μs/sample) current-stimulated DW displacement produced by a 2 μsec pulse.

The DW location within the polarimeter field-of-view prior to and after the current pulse are accurately measured (MOKE intensity); the DW displacements exhibit stochastic properties, which are discussed later. Averaged DW displacements scale with current density above j_t and appear to be independent of pulse duration for current pulse widths greater than 1 μsec (refer to 2 and 5 μsec displacements, Fig. 5.4).

Averaged DW displacements at $j = 4 \times 10^{11}$ A/m^2 are $\Delta x \sim 5$ μm and occur on a time scale of 0.3 μs (or faster). This result allows a lower limit to be placed on the measured average velocity $v_{min} \cong 5$ μm/0.3 μs $\cong$ 15m/sec. This result is significantly higher than (average) DW velocities obtained in prior experiments [66-68]. The corresponding efficiency is also higher, ∈ ~ 1.

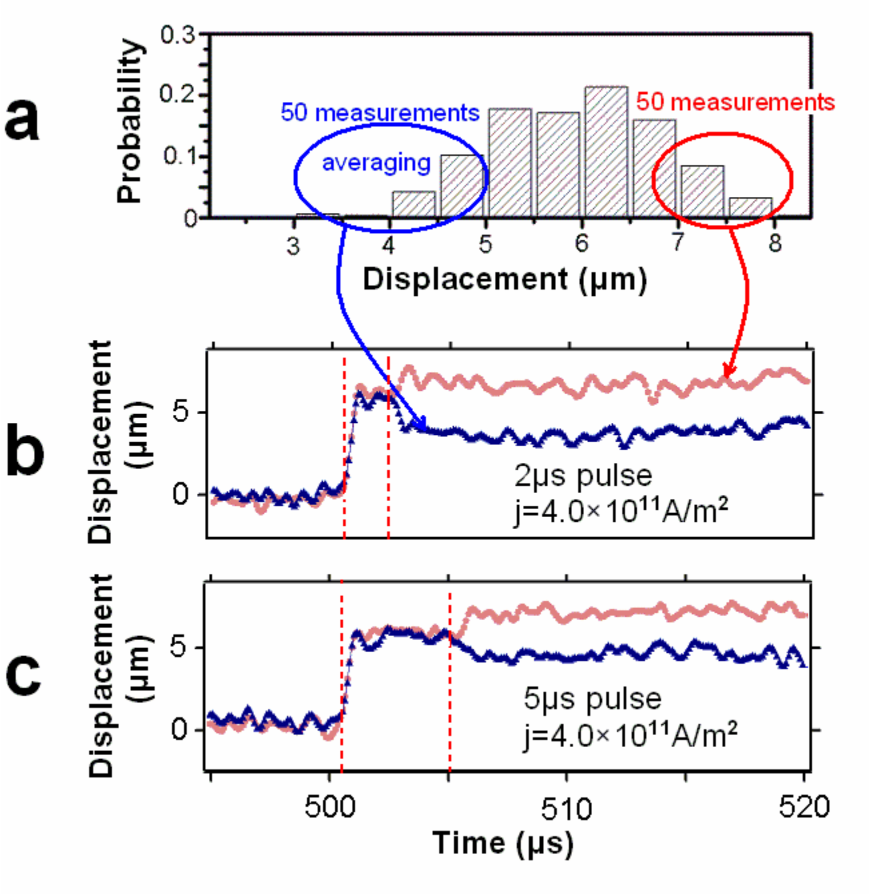

Figure 5.4: Panel a: statistical distribution of DW displacements after 500 measurements for 2μs pulses. Panels b and c: typical signal-averaged time-resolved DW displacements for two current pulse widths selected to illustrate positive and negative displacement relaxation effects at the pulse termination, associated with upper (light, red dots) and lower (dark, blue triangles) regions of the distribution (refer to text).

Figure 5.4 provides insight into the stochastic variations in current-driven DW displacements resulting from pulse excitation observed in prior experiments [66, 67] and in the present experiment. The DW displacements are calculated by averaging 2000 0.1 μsec samples prior to a specific M transient (Fig. 5.3a) and 2000 samples after the transient, and subtracting these two averages. The Gaussian-like distribution (Fig. 5.4a) from a total of 500 measurements manifests the non-deterministic nature of pulse-current-driven DW displacements between pinning centers. Additional information about the dynamics can be obtained by signal averaging the magnetic transients selected from the upper and lower tails of the distribution (Fig. 5.4a). Note that the noise for a single time-resolved displacement measurement at high temporal resolution (Fig. 5.3) is too large to resolve any details of the DW dynamics other than the prompt displacement initiated by the current step. Figures 5.4b and 5.4c display averages (50 measurements) of time-resolved DW displacements for 2μs pulses (distribution Fig. 5.4a) and 5μs pulses (distribution not shown) in which the signal-averaged trace by triangles in each panel was obtained by selecting displacement records from the lower tail of the distribution and the trace defined by circles was obtained from corresponding displacement records from the upper tail. All time-resolved DW displacements exhibit the same behavior: 1) an abrupt initial displacement in the direction of electron transport triggered by the leading edge of j(t) (this displacement increases with the increase of current density, Fig. 5.3c); and 2) a second abrupt smaller displacement in either direction at the termination of the pulse (the magnitude of this displacement also increases with current density). The initial displacement is nearly constant for pulses of variable width having the same current density, while both amplitude and direction of the second displacement is random. The Gaussian-like distribution (upper panel, Fig. 5.4) is mainly due to the second displacement. Careful analysis of the averaged time-resolved DW position after the initial prompt displacement but prior to the pulse termination show no evidence of a significant non-adiabatic contribution to DW displacement (which would manifest an additional systematic wall displacement in the direction of electron flow during the pulse). However the jumps at the termination of j(t) do suggest the presence of a (non-adiabatic) force of strength insufficient to overcome pinning.

Recent work by Thomas et al [82] detected and characterized oscillatory dependence of current-driven DW displacements on current pulse duration. In those experiments, the bi-directional displacements were shown to result from the oscillation of the probability of dislodging a DW confined to a pinning center by a very short (ns duration) current pulse.

Our experiments reveal a second mechanism that can produce bi-directional stochastic DW displacements stimulated at the termination of a (long duration) current pulse. LLG simulations of vortex-wall dynamics in Permalloy nanowire structure under high-field or current-drive conditions reveal motion in which the vortex core sweeps across the wire cross section perpendicular to the axis as it is driven along the wire in the direction of current or applied field [75]. Depinning and pinning of the vortex core occurs at the wire edges and the motion shows oscillation. We attribute the stochastic displacements of the wall at the termination of the current pulse to relaxation of the pinned vortex structure to a lower energy pinned state when $j = 0$ occurs.

To test the idea above, we did dynamic simulations for DW relaxation by a commercial simulator [83], which is based on LLG equation. Figure 5.5 shows the simulation results. Initially, a transverse DW is driven by a field of 75 Oe and the DW changes to a vortex structure as described above. On the left panel, the applied field is terminated at time t and the relaxation makes the DW center move down ward. On the right panel, the applied field is terminated 100ps later (t+100ps) and the relaxation makes the DW center move upward.

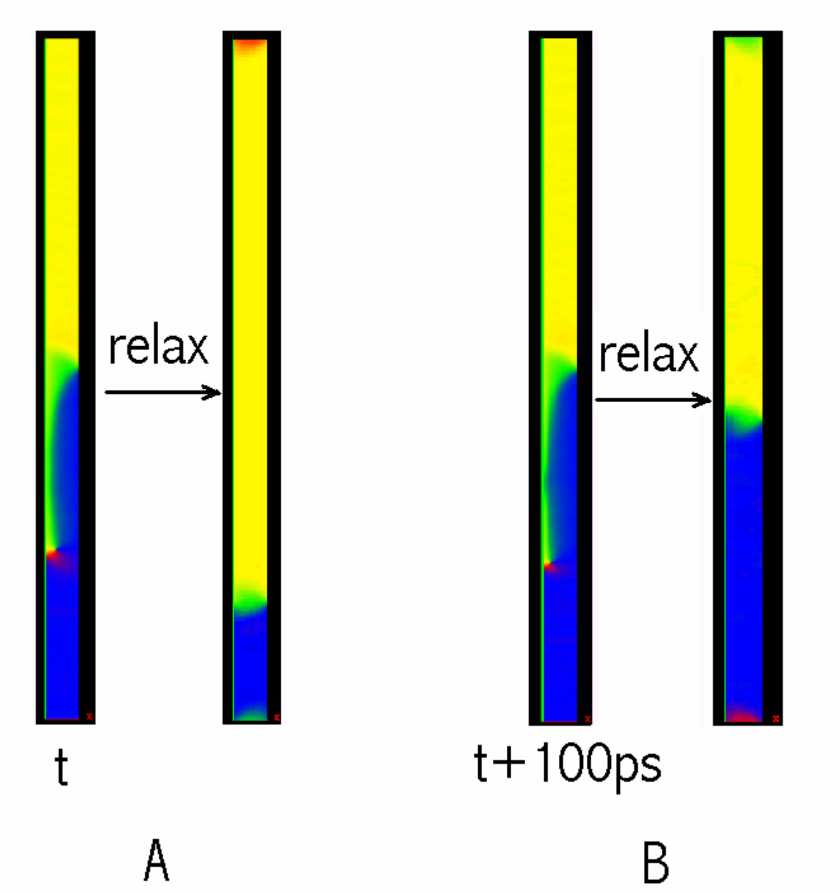

Figure 5.5: Simulation of the relaxation of a DW driven by a field of 75 Oe in a Permalloy sample (thickness = 5nm, width = 200nm, length = 4000nm) . Panel A: At time t, terminate the field and the relaxation makes the DW center move downward. Panel B: At time t+100ps, terminate the field and the relaxation makes the DW center move upward.

Although this simulation is for field only driven DW relaxation, it is possible that similar behavior also occurs for spin-transfer-torque-driven DWs and this can account the random relaxation in Figure 5.4.

5.4 Additional Experiments

In the experiment above, we did high temporal resolution MOKE measurements. However, due to the bandwidth limit, the temporal resolution is limited at about 300ns and we can only estimate the lower limit of the DW velocity, therefore further information of the DW motion is still not available. In this section we report an experiment beyond the temporal limit of 300ns. This experiment is still based on the MOKE technology above; however we can reach much higher temporal resolution by measuring DW displacements versus pulse duration, where the pulse duration can be tuned precisely.

The basic setup of this experiment is similar to Figure 5.2. Here we measure a permalloy wire with width = 800nm and thickness = 30nm. Again, the DW displacements are calculated by averaging 2000 0.1 μsec samples prior to a specific M transient (Fig. 5.3a) and 2000 samples after the transient, and subtracting these two averages. By this method we can obtain the DW displacement precisely.

The specific procedures are listed below: (i) A DW is prepared at the initial position. (ii) A current pulse with width "T" is applied on the Py wire and the DW displacement is measured. (iii) Increase the pulse width to "T + T" and repeat step (i) and (ii). These procedures are shown in Figure 5.6.

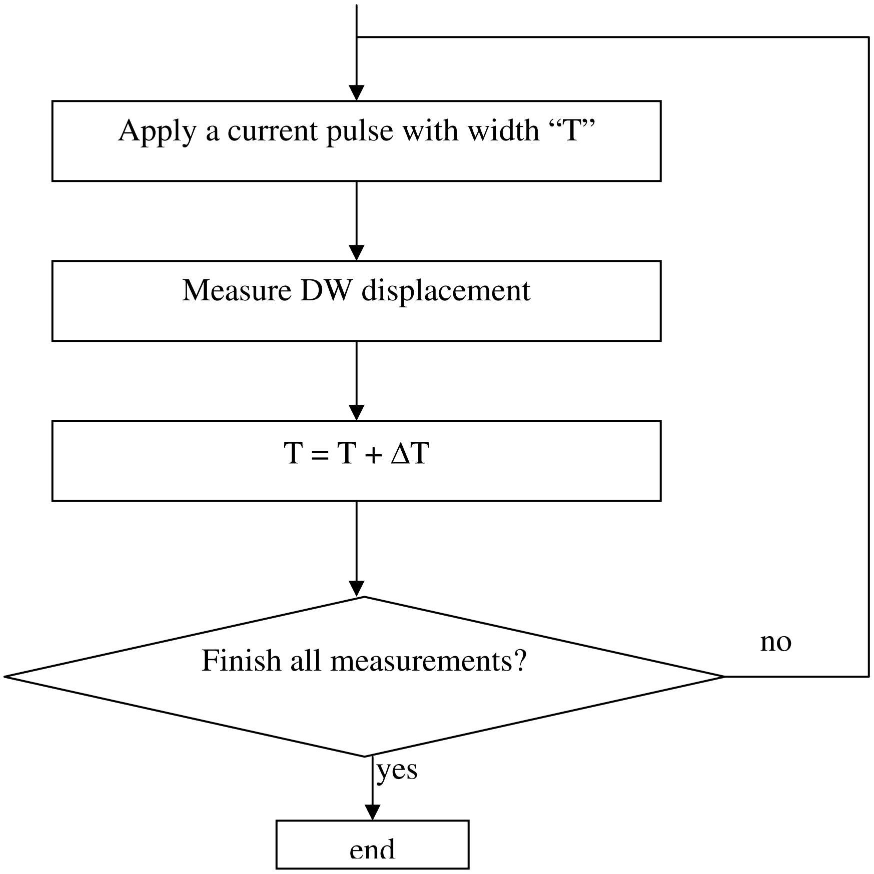

Figure 5.6: Procedures for DW displacement ~ pulse width experiments.

When ΔT is sufficiently small, we can map the DW displacement versus pulse width systematically and ΔT can be considered as the temporal resolution. In this experiment, the minimum ΔT is 25ns. The DW velocity can be calculated by ($\Delta d/\Delta T$), where Δd is the change of displacement. Figure 5.7 shows the data taken with different pulse voltage. (Due to the Joule heating, the current density is not a constant because of temperature relaxation. Therefore we use pulse voltage instead of current density here.) To reduce noise, every data point in the figure is from the average of 50 measurements under the same conditions. In the left-bottom of the figure, we use two pulses to schematically show how the data is taken.

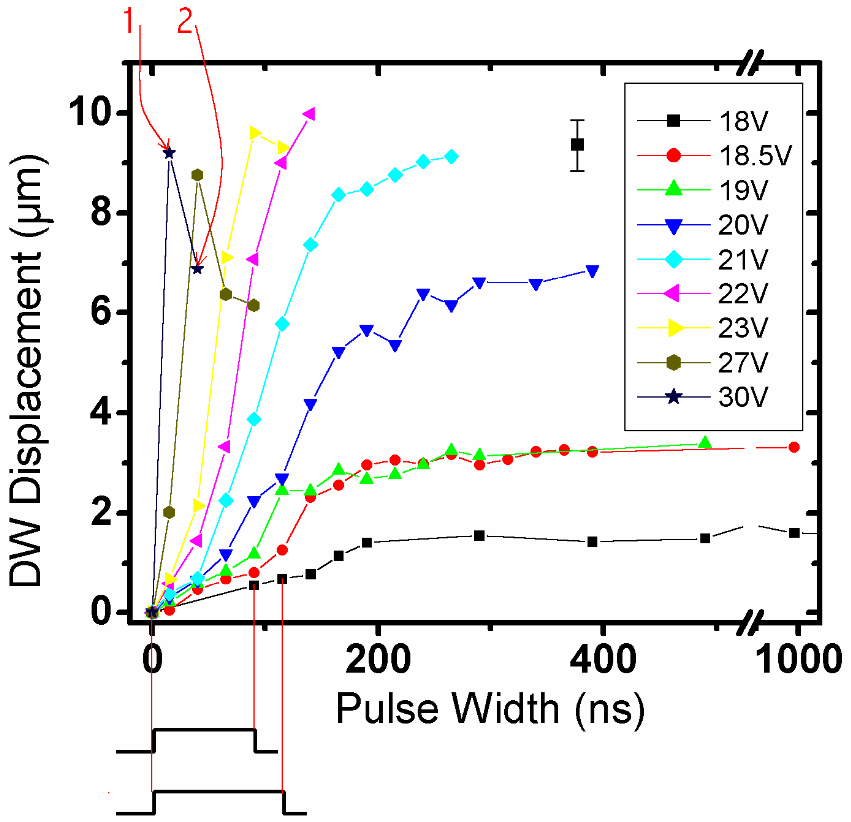

Figure 5.7: DW displacement versus current pulses at different voltage.

From Figure 5.7 we can get some features of the DW motion: (1) The DW only moves during about the first 200ns, and then it is pinned. This feature is consistent with the results in the section 5.3. It is not clear that the mechanism responsible for this phenomenon is the one described by Li and Zhang [60]. Defect pinning probably plays an important role. (2) The DW velocity increases rapidly as a function of the applied voltage, when the voltage is beyond a threshold value (~18V). (3) At low voltage (<20V), the DW velocity is “normal”, because the spin-flip efficiency is less than 1, where spin-flip efficiency is defined as the ratio of number of flipped spin over number of electron transferred by current and it should be less than one. Figure 5.8b shows a DW after applying a pulse of 19V and 300ns. The DW is not a single vortex as the initial one. This phenomenon was reported before [84]. (4) At higher voltage, the DW velocity is so high that the spin-flip efficiency can be much larger than 1. For instance, the arrow-1 in Figure 5.7 indicates a pulse of 30V and 15ns and the velocity is about 600m/s. Figure 5.8c shows a MFM image after such a pulse. A complex domain structure is formed in the wire. Arrow-2 indicates a data from 40ns pulse under the same voltage. The decrease of DW displacement implies that the temperature during the pulse is beyond Curie temperature.

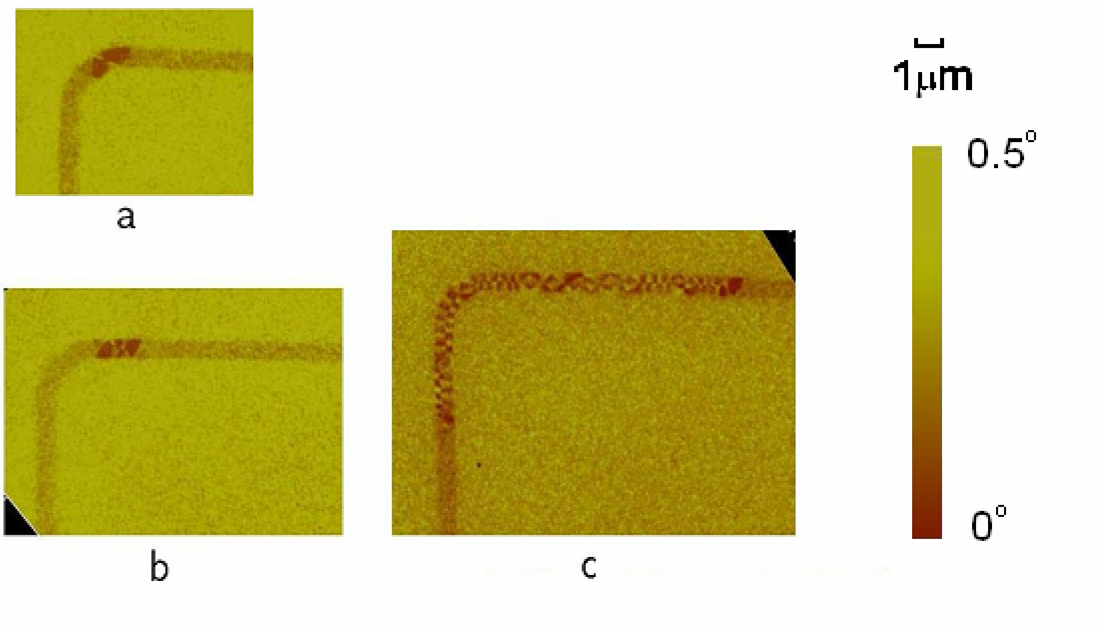

Figure 5.8: MFM images of DW structures (a) A DW prepared at the initial

position. (b) A DW after applying a pulse of 19V and 300ns. (c) Domain structures after a pulse of 30V and 15ns

5.5 Conclusion

In summary, this chapter presents time-resolved measurements of pulse-current-driven DW displacements in nanometer-scale Permalloy wires that manifest prompt motion wall velocities exceeding 15 m/sec at $j = 4 \times 10^{11}$ A/m^2 and spin-flip efficiencies $\in \sim 1$. These values are a factor of ten higher than indicated in prior experiments, which have been interpreted to suggest that the adiabatic mechanism cannot explain pulse-driven DW dynamics. Most of the measured displacements occur within 0.3 μsec of the leading edge of the pulse and careful analysis of the wall position after the initial displacement (while current persists) shows no evidence of sustained motion that would occur if a significant non-adiabatic term contributed to wall displacement. The sample temperature was evaluated during the applied current pulses and it was shown that the steady-state temperature remains significantly below the Curie temperature for Permalloy. These results suggest that the adiabatic spin-torque mechanism is a viable mechanism for the observed current-driven DW depinning and prompt displacements, and that spin-wave creation associated with depinning is not responsible for low spin-flip efficiencies determined from prior experiments. The DW displacement effects at the pulse termination suggest the presence of a non-adiabatic force that is too weak to overcome pinning, but could maintain significant DW distortion that relaxes when the current is terminated. This is supported by simulations for field-driven domain-wall relaxation.

Additional experiments are carried out by the measurement of DW displacement versus pulse width at different excitation voltages. Higher temporal resolution can be achieved by the variation of pulse width and the DW velocities can be obtained by the slope of the displacement – pulse-width curves. The data confirms that the DW displacement does not scale with pulse width. MFM images are also taken to study DW displacements and domain structures. At lower voltage, the DW remains intact, while it can be a multi-vortex DW. At high voltage, the velocity can be very high and the effective spin-flip efficiency is much larger than 1, while complex domain structure appears.

Bibliography

[1] S. A. Wolf et al., *Science* **294**, 1488 (2001).

[2] P.Weiss, J. de Phys. 6, 661 (1907).

[3] W. Heisenberg, Z. Phys. 38, 441 (1926).

[4] W. F. Brown, Jr.: Micromagnetics (Wiley, New York, 1963).

[5] L. D. Landau and E. Lifshitz: On the theoty of the dispersion of magnetic permeability in ferromagnetic bodies. Phys. Z. Sowjetunion 8, 153-169 (1935)

[6] C. H. Marrows, Advances in Physics,Vol. 54, No. 8, 585, 2005.

[7] A. Hubert and R. Schafer, Magnetic Domains The analysis of Magnetic Microstructures (Springer-Verlag Berlin Heidelberg, New York, 1998).

[8] H. Barkhausen, Z. Phys. **20**, 401 (1919).

[9]G. Durin and S. Zapperi, Cond-mat/0404512 (2004).

[10] B. Alessandro, C. Beatrice, G. Bertotti and A, Montorsi, J. Appl. Phys. **68**, 2901 (1990); **68**, 2908 (1990).

[11] P. Cizeau, S. Zapperi, G. Durin and H.E. Stanley, Phys. Rev. Lett. **79**, 4669 (1997); Phys. Rev. **B58**, 6353 (1998).

[12] G. Bertotti, G. Durin and A. Magni, J. Appl. Phys. **75**, 5490 (1994).

[13] G. Bertotti, Hysteresis in Magnetism (Academic Press, San Diego, 1998).

[14] A. Magni, C. Beatrice, G. Durin, and G. Bertotti, J. Appl. Phys. **86**, 3253 (1999).

[15] C. Nistor, E. Faraggi and J. L. Erskine, Phys. Rev. **B72**, 014404 (2005).

[16] J.S. Urbach, R.C. Madison, and J.T. Markert, Phys. Rev. Lett. **75**, 276 (1995); **75**, 4694 (1995).

[17] H.J. Williams, W. Shockley and C. Kittel, Phys. Rev. **80**, 1090 (1950).

[18] R.M. Bozorth, Ferromagnetism, VanNostrand Company Inc. New York (1961).

[19] M. Heidkamp and J.L. Erskine, Rev. Sci. Instrum. **71**, 3141 (2000).

[20] E. Puppin, Phys. Rev. Lett. **84**, 5415 (2000).

[21] L. Callegaro, E. Puppin, and S. Ricci, J. Appl. Phys. **90**, 2416 (2001).

[22] O. Perkovic, K. Dahmen and J. P. Sethna, Phys. Rev. Lett. **75**, 4528 (1995).

[23] A. Vazquez and Q. Sotolongo-Costa, Phys. Rev. Lett. **84**, 1316 (2000).

[24] R. A. White and K. A. Dahmen, Phys. Rev. Lett. **91**, 085702-1 (2003).

[25] S. L. A. deQueiroz, Phys. Rev. E **69**, 026126 (2004).

[26] P. Bak, C. Tang, and K. Wiesenfeld, Phys. Rev. Lett. **59**, 381 (1987).

[27] N. J. Wiegman, Masters Thesis, Technische Universiteit, Eindhoven; (results described in Ref. 9.)

[28] E. Puppin, S. Ricci, and L. Callegaro, Appl. Phys. Lett. **76**, 2418 (2000).

[29] D.-H. Kim, S.-B. Choe, and S.-C. Shin, Phys. Rev. Lett. **90**, 087203-1 (2003).

[30] M. Redjdal, J. Giusti, M. Ruane and F.B. Humphrey, J. Appl. Phys. **91**, 7547 (2002).

[31] Y. Nakatani, N. Hayashi, T. Ono and H. Miyajima, IEEE Trans. Mag. **37**, 2129 (2001).

[32] T.J. Silva, C.S. Lee, T.M. Crawford and C.T. Rogers, J. Appl. Phys. **85**, 7849 (1999).

[33] W.K. Hiebert, A. Stankiewicz and M.R. Freeman, Phys. Rev. Lett. **78**, 1134 (1997).

[34] G. S. D. Beach, C. Nistor, C. Knutson, M. Tsoi, and J. L. Erskine, *Nature Mater.* **4**, 741 (2005).

[35] Y. Nakatani, A. Thiaville, and J. Miltat, Nature, 194-196, 1009 (1994).

[36] S. Konishi, S. Yamada, and T. Kasnda, IEEE Trans. Magn. MAG-7, 722 (1971).

[37] P. Vavassori, F. Ronconi, M. Traldi, and E. Puppin, J. Mag. Mag. Matl. **177/178**, 127 (1998).

[38] T.A. Moore, J. Rothman, Y.B. Xu, and J.A.C. Bland, J. Appl. Phys. **89**, 7018 (2001).

[39] W.Y. Lee, B.-Ch. Choi, Y.B. Xu, and J.A.C. Bland, Phys Rev. **60**, 10, 216 (1999).

[40] L. Sauti, R. L. Sommer, A. Magni, G. Durin, F. Colaiori, and S. Zapperi, IEEE Trans. Magnetics **39**, 2666 (2003).

[41] I. Lyuksyutov, T. Natterman, and V. Pokrovsky, Phys. Rev. **B39**, 4260 (1999).

[42] M. Kolesik, M.A. Novotny and P.A. Rikvold, Phys. Rev. **B56**, 11,791 (1997).

[43] T.A. Moore, S.M. Gardiner, C.M. Guertler, and J.A.C. Bland, Physica **B343**, 337 (2004).

[44] G. Durin and S. Zapperi, cond-mt/0404512.

[45] J. P. Sethna, K. A. Dahmen and C. R. Meyers, Nature **410**, 242 (2001).

[46] A. Zentko and V. Hajko, Czech. J. Phys **B18**, 1026 (1968).

[47] R. Becker, Z. Phys. **62**, 253 (1930).

[48] L. V. Kirensky and W. F. Ivlev, Dokl. Akad. Nank SSSR **76**, 389 (1951). [Sov. Phys. Dok.] 1, 1 (1956).

[49] V. Hajko, A. Zentko and S. Filka, Czech. J. Phys. **B19**, 547 (1969).

[50] M. Zani and E. Puppin, J. Appl. Phys. **94**, 5901 (2003).

[51] J. Kranz and A. Schauer, Ann. Phys. **7**, 84 (1959).

[52] A. Zentkova, A. Zentko and V. Hajko, Czech. J. Phys. **B19**, 547 (1969).

[53] This experiment was alluded to in ref. 52.

[54] A. Zentkova, Czech. J. Phys. Sect. **B19**, 1454 (1969).

[55] R. D. Gomez, T. V. Luu, A. D. Pak, I. D. Mayergoyz, K. J. Kirk, and J. N. Chapman, J. Appl. Phys. **85**, 4598 (1999).

[56] M. Bartheimess, C. Pels, A. Thieme, and G. Meier, J. Appl. Phys. **95**, 5641 (2004).

[57] G. A. Prinz, Science **282**, 1660 (1998).

[58] D. A. Allwood et al., Science **309**, 1688 (2005).

[59] G. Tatara and H. Kohno, Phys. Rev. Lett. **92**, 086601 (2004).

[60] Z. Li and S. Zhang, Phys. Rev. Lett. **92**, 207203 (2004).

[61] S. Zhang and Z. Li, Phys. Rev. Lett. **93**, 127204 (2004).

[62] Z. Li and S. Zhang, Phys. Rev. B **69**, 134416 (2004).

[63] Z. Li and S. Zhang, Phys. Rev. B **70**, 024417 (2004).

[64] A. Thiaville, et al., J. Appl. Phys. **95**, 7049 (2004).

[65] J. Xiao, A. Zangwill and M.D. Stiles, Phys. Rev. B **73**,054428 (2006).

[66] A. Yamaguchi, et al., Phys. Rev. Lett. **92**, 077205 (2004).

[67] A. Yamaguchi, et al., Appl. Phys. Lett. **86**, 012511 (2005).

[68] M. Kläui, et al., Phys. Rev. Lett. **95**, 026601 (2005).

[69] S. H. Florez, et al., J. Appl. Phys. **97**, 10C705 (2005).

[70] C. K. Lim, et al., Appl. Phys. Lett. **84**, 2820 (2004).

[71] L. Berger, J. Appl. Phys. **49**, 2156 (1978).

[72] L. Berger, J. Appl. Phys. **55**, 1954 (1984).

[73] L. Berger, J. Appl. Phys. **71**, 2721 (1992).

[74] D. Atkinson, et al., Nature Mater. **2**, 85 (2003).

[75] Y. Nakatani, et al., Nature Mater. **2**, 521 (2003).

[76] M. D. Stiles et al. (unpublished).

[77] G. S. D. Beach, et al., Phys. Rev. Lett. **97**, 057203 (2006).

[78] M. Hayashi et al., Phys. Rev. Lett. **96**, 197207 (2006).

[79] M. Klaui, et al., Appl. Phys. Lett. **85**, 5637 (2004).

[80] Y. Nakatani, et al., J. Mag. Mag. Mat. **290**, 750 (2005).

[81] R. M. Bozorth, Ferromagnetism, D. Van Nostrand Company, Inc., Princeton (1951).

[82] L. Thomas et al., Nature, **443** (7108): 197-200 (2006).

[83] LLG micromagnetic software, developed by M. Scheinfein.

[84] M. Klaui, et al. Applied Physics Letters 88, 232507 2006.

[85] Shuqiang Yang and J.L. Erskine, Phys. Rev. B, 72 (6) 064433, 2005

[86] Shuqiang Yang, G.S.D.Beach and J.L. Erskine, Journal of Applied Physica 100(11) 113914, 2006

[87] Shuqiang Yang and J.L. Erskine, Physical Review B. 75, 220403, 2007

Vita

Shuqiang Yang was born in Jinan, Shandong Province, China, on November, 2nd, 1973, the son of Sumei Shi and Jinyin Yang. He entered Shandong University in September 1992 and graduated with a Bachelor of Science in Physics in June 1996. Then he was enrolled in Institute of Physics, Chinese Academy of Science and received a Master of Science degree in Electronics in August 1999. In January 2001 he entered the graduate school at the University of Texas at Austin.

Permanent Address: 73 Village Lane Apt. 606, Wethersfield, CT 06109

This dissertation was typeset by the author.